Fermionic signal of vacuum polarization in strong laser fields

Ya-Nan Dai,[1] Karen Z. Hatsagortsyan,[2,*] Christoph H. Keitel,[2] and Yue-Yue Chen[1,†]
[1]*Department of Physics, Shanghai Normal University, Shanghai 200234, China*
[2]*Max-Planck-Institut für Kernphysik, Saupfercheckweg 1, 69117 Heidelberg, Germany*

(Received 20 January 2024; accepted 31 May 2024; published 11 July 2024)

Vacuum polarization (VP) is investigated for the interaction of a polarized γ-ray beam of GeV photons with a counterpropagating ultraintense laser pulse. In a conventional setup of a vacuum birefringence measurement, a VP signal is the emerging small circular (linear) polarization of the initially linearly (circularly) polarized probe photons. The pair production via the nonlinear Breit-Wheeler process in such a high-energy environment eliminates part of the γ photons in the outgoing γ beam, increasing the statistical error and decreasing the accuracy of this VP signal. In contrast, we investigate the conversion of the emerging circular polarization of γ photons into longitudinal polarization of the created positrons, considering the latter as the main VP signal. To study the VP effects in the highly nonlinear regime, where the Euler-Heisenberg effective Lagrangian method breaks down, we have developed a Monte Carlo simulation method, incorporating vacuum birefringence and dichroism via the one-loop QED probabilities in the locally constant field approximation. Our Monte Carlo method will enable the study of VP effects in strong fields of arbitrary configuration. With 10 PW laser systems, we demonstrate the feasibility of detecting the fermionic signal of the VP effect at the 5σ confidence level with a few hours of measurement time.

DOI: 10.1103/PhysRevD.110.012008

I. INTRODUCTION

Quantum electrodynamics predicts virtual electron-positron pair creation by a photon in vacuum, resulting in vacuum polarization (VP) in strong electromagnetic fields and the quantum vacuum behaving as a birefringent medium [1–3]. This intriguing phenomenon has not been directly proven in an experiment despite continuous attempts [4–7]. This is important not only as a proof of nonlinear QED, but also it may point towards new physics beyond the standard model [8–11].

The vacuum birefringence (VB) signal is enhanced using stronger background fields, longer interaction distances, and a higher probe frequency, and the main hindering factor is the background noise. The long interaction distance has been implemented in PVLAS [12,13] and BMV [5] experiments, which aim to measure the ellipticity acquired by a linearly polarized optical light propagating through a strong static magnetic field (8.8 T) of a long extension (1 m), however, without conclusive results so far [4].

*Contact author: k.hatsagortsyan@mpi-hd.mpg.de
†Contact author: yue-yue.chen@shnu.edu.cn

The advent of high-intensity optical [14,15] and x-ray free-electron lasers (XFEL) [16], coupled with rapid advancements in x-ray polarimetry (with achievable precision of 8×10^{-11} [17]), has opened new perspectives for measuring VB with the use of ultrastrong laser fields (with magnetic fields reaching 10^6 T) and keV photons of XFELs [18–22]. Using a 10 petawatt (PW) class laser, the induced ellipticity signal can reach up to $\sim 10^{-4}$ for the XFEL probe [22]. The HIBEF consortium is developing the flagship experiment in this regime [23].

Further enhancement of the VB signal is envisaged for a combination of γ-ray sources [24] and PW laser facilities [25–28]. The ultrastrong laser fields can also be replaced by the fields of an aligned crystal [29]. The common VB signal discussed in this setup is the polarization of the γ-ray beam after the interaction, which relies on the feasibility of sensitive γ-ray polarimetry, which is a challenging task [27]. In the VB setup via laser-γ-beam collisions, copious real pairs are produced due to nonlinear Breit-Wheeler process, which is the source of vacuum dichroism (VD) [28]. This effect is especially dramatic when the quantum nonlinearity parameter is large $\chi_\gamma \gtrsim 1$ [30]. The pair production decreases the number of γ photons in the final state, increasing the statistical error of the VB signal measurement, thus playing the role of undesirable noise.

While in the case of optical and x-ray probes the treatment of VB is valid within the Euler-Heisenberg effective Lagrangian method, as the probe photon energy

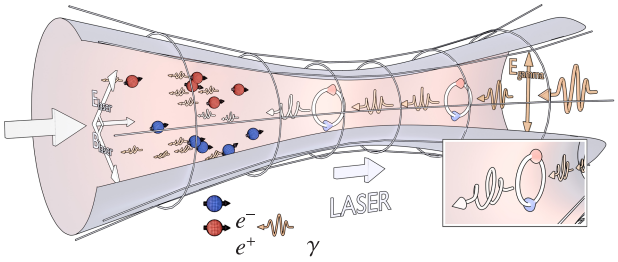

FIG. 1. Measurement scheme for VP: γ photons of linearly polarized penetrate a strong counterpropagating laser pulse, with linearly polarized aligned at 45 deg with respect to the γ polarization. The γ photons develop circular polarization due to VB and align along the electric field due to VD. Subsequently, the circular polarization of γ photons is transformed into the longitudinal polarization of electrons and positrons as generated in the nonlinear Breit-Wheeler process, yielding a discernible fermionic signal of VP.

is negligible with respect to the electron rest mass, the QED photon polarization operator in the strong background field should be employed in the case of a γ probe. The QED polarization operator within one-loop approximation has been investigated in Refs. [30–34], which has been applied to the VP problem [28,35]. In particular, in Ref. [28], the feasibility of detecting VB and VD with 10 PW laser systems and GeV γ photons on the timescale of a few days was demonstrated. For VB in a crystal, circular polarization of ∼18% is obtained with incident photons in the energy range of 180 GeV [29]. Recently, it has been proposed to use helicity flips to detect VB [35]; however, the obtained signature is of high order (α^2) in the fine structure constant α, with a suppressed probability.

In this paper, we put forward a method for observing VB via the created *positron* longitudinal polarization during the interaction of linearly polarized γ photons with a linearly polarized ultraintense laser pulse in the highly nonlinear regime with $\chi_\gamma \gtrsim 1$. We employ a general scheme of the pioneering experiment E-144 at stanford linear accelerator center [36–39], to produce γ photons via Compton scattering and further convert them into electron-positron pairs in an ultrastrong laser field using the nonlinear Breit-Wheeler process. However, we add a polarization perspective to this seminal scheme to exploit it for the application of a VB measurement. Here, the initially linearly polarized γ photons propagate in a PW laser pulse, acquiring circular polarization due to VP. The helicity of the photons is subsequently transferred to the produced pairs during the nonlinear Breit-Wheeler process, generating longitudinally polarized positrons with polarization up to ∼70%. Therefore, rather than the conventional *photonic signal* of VP, we find a strong signature of VB in the *positron polarization*; see the scheme of the interaction in Fig. 1. In contrast to previous schemes where the pair production is undesirable, increasing the statistical error of the VB measurement, we employ the pairs as a source for a valuable VB signal. To carry out the investigation, we have developed a Monte Carlo method for the simulation of VB and VD of a γ-ray beam in a highly nonlinear regime, which applies to an arbitrary configuration of a background strong field. We demonstrate the experimental feasibility of our proposal for measuring VB with an average statistical significance of 5σ on the measurement timescale of a few hours in upcoming 10 PW laser facilities.

II. VACUUM BIREFRINGENCE AND DICHROISM

Let us first introduce our Monte Carlo method, which allows us to treat the γ-photon polarization dynamics induced by the VB and VD in the strong field of arbitrary configuration. Until now, the QED Monte Carlo method is known for the simulation of the photon emission and pair production processes [40–47], which employ the polarization resolved probabilities of the photon emission and pair production in strong fields via the tree diagrams in the locally constant field approximation; see the overview in Ref. [48]. The loop diagram contribution of the order of α via the interference of the one-loop self-interaction with the forward scattered one is also included for the electron, describing the so-called no-photon emission probabilities for the electron polarization change [34,49]. However, the similar loop diagram contributions for a photon polarization change were missing in the present QED Monte Carlo codes and have been implemented in this work.

The impact of radiative corrections to photon polarization includes a polarization generation of ξ_3 associated with VD and a rotation of $\xi_\perp = (\xi_1, \xi_2)$ induced by VB, where $\boldsymbol{\xi}_i = (\xi_1, \xi_2, \xi_3)$ are the Stokes parameters of the incident photons. The former corresponds to the imaginary part of polarization operator, which is related to the pair production probability via the optical theorem, and the latter corresponds to the real part of the polarization operator. The polarization variation of a photon propagating in a background field is described by the Feynman diagrams shown in Fig. 2. Panel (a) shows the probability via the tree-level propagation diagram, being zeroth order in the fine structure constant α. Panel (b) presents the probability via the interference diagram of the tree-level propagation diagram and the one-loop propagation diagram, being first order in α. The results of the QED calculations up to the $O(\alpha)$-order loop contribution [34] are presented in Appendix A. The first term P^L_{VD} of Eq. (A4) describes VD, while the second one P^L_{VB} is related to VB.

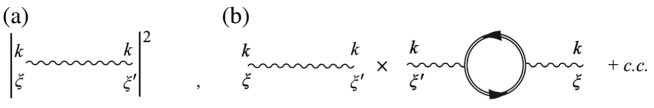

FIG. 2. Diagrams contributing to polarization variation of a photon: (a) zeroth order in α, the tree-level propagation diagram, and (b) first order in α, interference diagram of the tree-level propagation diagram and the one-loop propagation diagram.

A. Photon polarization due to the no-pair production probability

The polarization change due to VD arises because photons with different polarization states are absorbed via pair production differently during propagation. In other words, the dependence of pair production probability by a photon on the photon polarization will result in the polarization variation of the total photon beam. This selection effect is termed as the change of the photon polarization state during the no-pair production process. We derive below the "no-pair production" probability and use it in our modified Monte Carlo code to describe VD.

We begin with the probability for pair production

$$dW^P = \frac{\alpha m^2 d\varepsilon}{\sqrt{3}\pi\omega^2}\left\{\int_{z_p}^{\infty} dx \mathrm{K}_{\frac{1}{3}}(x) + \frac{\varepsilon_+^2+\varepsilon^2}{\varepsilon\varepsilon_+}\mathrm{K}_{\frac{2}{3}}(z_p) - \xi_{i3}\mathrm{K}_{\frac{2}{3}}(z_p)\right\}, \tag{1}$$

where ξ_{i3} is the Stokes parameter for linear polarization along polarization basis $\hat{\mathbf{e}}_1 = (1,0,0)$ and $\hat{\mathbf{e}}_2 = (0,1,0)$. The no-pair production probability obtained from the probability conservation is

$$\begin{aligned} w^{NP}(\boldsymbol{\xi}_i) &= 1 - \{\underline{w} + \underline{\boldsymbol{f}}\cdot\boldsymbol{\xi}_i\}\Delta t, \\ \underline{w} &= \int \frac{\alpha m^2 d\varepsilon}{\sqrt{3}\pi\omega^2}\left[\int_{z_p}^{\infty} dx \mathrm{K}_{\frac{1}{3}}(x) + \frac{\varepsilon_+^2+\varepsilon^2}{\varepsilon\varepsilon_+}\mathrm{K}_{\frac{2}{3}}(z_p)\right], \\ \underline{\boldsymbol{f}} &= -\int \frac{\alpha m^2 d\varepsilon}{\sqrt{3}\pi\omega^2}\hat{e}_3 \mathrm{K}_{\frac{2}{3}}(z_p). \end{aligned} \tag{2}$$

The dependence of pair production probability on photon polarization ξ_{i3} results in a preference of the final polarization state (see also the discussion at Eq. (5.12) in Ref. [50]). Because of this selection effect of initial photon polarization, the final polarization vector after the no-pair production process becomes

$$\boldsymbol{\xi}_f^{\boldsymbol{NP}} = \frac{\boldsymbol{\xi}_i(1-\underline{w}\Delta t) - \underline{\boldsymbol{f}}\Delta t}{1-\{\underline{w}+\underline{\boldsymbol{f}}\cdot\boldsymbol{\xi}_i\}\Delta t} = \frac{\boldsymbol{d}^{NP}}{c^{NP}}. \tag{3}$$

We can estimate the polarization variation induced by the no-pair production process as $\Delta\xi_{NP} = w^{NP}(\boldsymbol{\xi}_i)(\boldsymbol{\xi}_f^{\boldsymbol{NP}} - \boldsymbol{\xi}_i)$ and derive the equation for the corresponding evolution of Stokes parameters:

$$\frac{d\boldsymbol{\xi}_{NP}}{dt} = \int \frac{\alpha m^2 d\varepsilon}{\sqrt{3}\pi\omega^2}(\hat{\mathbf{e}}_{\mathbf{3}} - (\boldsymbol{\xi}_i\cdot\hat{\mathbf{e}}_{\mathbf{3}})\boldsymbol{\xi}_i)\mathrm{K}_{\frac{2}{3}}(z_p). \tag{4}$$

Note that if the photon is in a pure state $\boldsymbol{\xi}_i = \pm\hat{\mathbf{e}}_{\mathbf{3}}$ then there is no polarization variation induced by no-pair production process. If the photon is in a mixed state along $\hat{\mathbf{e}}_{\mathbf{3}}$ or other directions other than $\hat{\mathbf{e}}_{\mathbf{3}}$, then

$$\begin{aligned} \frac{d\xi_1}{dt} &= -\int \frac{\alpha m^2 d\varepsilon}{\sqrt{3}\pi\omega^2}\xi_3\xi_1\mathrm{K}_{\frac{2}{3}}(z_p), \\ \frac{d\xi_2}{dt} &= -\int \frac{\alpha m^2 d\varepsilon}{\sqrt{3}\pi\omega^2}\xi_3\xi_2\mathrm{K}_{\frac{2}{3}}(z_p), \\ \frac{d\xi_3}{dt} &= \int \frac{\alpha m^2 d\varepsilon}{\sqrt{3}\pi\omega^2}(1-\xi_3^2)\mathrm{K}_{\frac{2}{3}}(z_p). \end{aligned} \tag{5}$$

B. Vacuum birefringence

The term P_{VB} in the loop contribution is associated with the real part of the polarization operator. It induces a retarded phase between the polarization components along the basis $\hat{\mathbf{e}}_1$ and $\hat{\mathbf{e}}_2$, resulting in a rotation between ξ_1 and ξ_2, and in this way contributing to VB. The full VB effect arises due to the net contribution of the α-order loop process and the pair-production tree process (with partial cancellation). In our simulation, the VB is realized by rotation of the photon polarization vector in (ξ_1,ξ_2) plane at each step [22,28,34] [see Eq. (A10)],

$$\begin{pmatrix}\xi_1^f\\ \xi_2^f\end{pmatrix} = \begin{pmatrix}\cos\varphi & \sin\varphi\\ -\sin\varphi & \cos\varphi\end{pmatrix}\begin{pmatrix}\xi_1\\ \xi_2\end{pmatrix}, \tag{6}$$

where $\varphi = \frac{\alpha m^2}{\omega^2}\Delta t\int d\varepsilon\frac{\mathrm{Gi}'(\xi)}{\xi}$, with $\xi = 1/[\delta(1-\delta)\chi_\gamma]^{2/3}$, $\delta = \varepsilon/\omega$, and $\mathrm{Gi}'(x)$ being the Scorer prime function.

C. Employed Monte Carlo simulation method for vacuum birefringence and dichroism

Our modified QED Monte Carlo code is augmented to include VB and VD via Eqs. (3) and (6) as described above. Thus, our Monte Carlo method provides the full account for the spin- and polarization-resolved tree process (nonlinear Breit-Wheeler) and the loop process (vacuum polarization). In our Monte Carlo code, at each simulation step Δt, the pair production is determined by the total pair production probability and the positron energy and polarization by the spin-resolved spectral probability [48], using the common algorithms [40–47]. If the pair production event is rejected, the photon polarization state is determined by the photon-polarization dependent loop probability w^{NP}. The full description of the Monte Carlo method is given in Appendix B.

Note that we are working in the regime of $\chi_\gamma \gtrsim 1$, $\alpha\chi^{2/3} \ll 1$, where recoil and pair production are important, but the radiation field is a perturbation. In our simulation, we take into account the α-order contributions, i.e., the tree-level first-order processes of photon emission (nonlinear Compton) and pair photoproduction (nonlinear Breit-Wheeler), as well as the one-loop radiative corrections to the electron self-energy (electron mass operator) and

photon self-energy (photon polarization tensor). The tree-level first-order processes are related to the one-loop self-energies by virtue of the optical theorem. In the considered regime, high-order radiative corrections are negligibly small. They become significant only when $\alpha\chi^{2/3} \gtrsim 1$ and are therefore not included in our code.

III. SETUP FOR THE DETECTION OF THE VACUUM POLARIZATION EFFECTS IN STRONG LASER FIELDS

A. Generating a linearly polarized γ-ray beam via linear Compton scattering

We assume that the probe γ photons are produced by linear Compton scattering of a linearly polarized laser pulse with intensity of $I \sim 10^{16}$ W/cm^2 ($a_0 = 0.1$) and pulse during of $\tau_p = 10$ ps. To derive the parameters of the probe γ-photon beam, we simulate the process with realistic incoming electron beam parameters according to Refs. [28,51]. The electron beam counterpropagating with the laser pulse consists of $N_e^0 = 2 \times 10^6$ electrons. The electron initial kinetic energy is 8.4 GeV, the energy spread $\Delta\varepsilon_0/\varepsilon_0 = 0.035$, and the angular divergence $\Delta\theta = 0.24 \times 10^{-3}$ mrad. The angular distribution and spectrum of emitted photons are obtained using CAIN code [50], which takes into account of the electron distribution, angular (energy) divergence of the electron beam, radiation reaction, and stochasticity of scattering events. The γ photons within $\theta_{\max} = 0.05$ mrad are highly polarized with $\bar{\xi}_i = (-0.91, 0, 0)$ and have an average energy of $\bar{\omega}_\gamma = 1.1$ GeV with energy spread $\Delta\omega_\gamma/\bar{\omega}_\gamma = 0.54$; see Fig. 3. The photon yield within $\theta \le \theta_{\max}$ is $N_\gamma = 1 \times 10^6 \approx 0.5 N_{e^-}^0$. The latter is in accordance with analytical estimations; see Appendix C. The γ-ray beam can be generated in a beamline similar to the beamline 2 of the Laser Electron Photon Experiment at SPring-8 (LEPS 2) [52], if an upgrade of the laser intensity up to $a_0 = 0.1$ and the electron angular divergence up to $\Delta\theta = 0.24 \times 10^{-3}$ mrad are implemented.

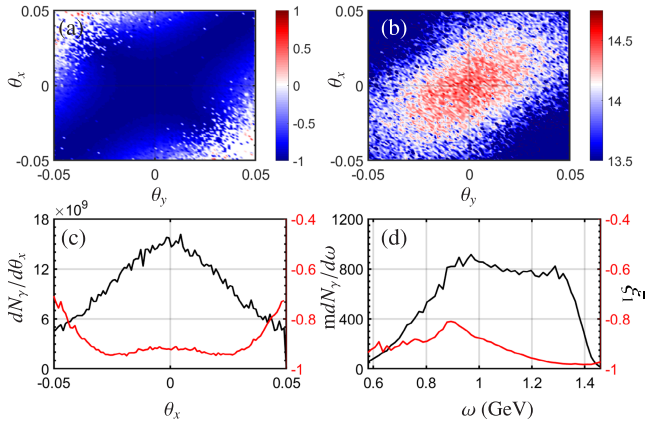

FIG. 3. (a) Angular distribution of γ photon density $\log_{10} d^2N/d\theta_x/d\theta_y$ (mrad^{-2}) and (b) polarization ξ_1 vs θ_x (mrad) and θ_y (mrad). (c) The angular distribution of γ photon density $dN_\gamma/d\theta_x$ (mrad^{-1}) (black solid line) and polarization ξ_1 (red solid line) vs θ_x. (d) The energy distribution of γ photon density $mdN_\gamma/d\omega$ (GeV^{-1}) (black solid line) and polarization ξ_1 (red solid line) vs ω(GeV).

B. Fermionic signal of vacuum polarization in strong laser fields

Afterward, these photons collide with a 10 PW laser beam for the high-energy VB and VD experiment. Here, we use a focused Gaussian linearly polarized laser pulse, with the peak intensity $I \sim 10^{23}$ W/cm^2 ($a_0 = 150$), wavelength $\lambda_0 = 800$ nm, pulse duration $\tau_p = 50$ fs, and the focal radius $w_0 = 5\lambda_0$ [53,54].

The simulation results for the final photons are shown in Figs. 4 and 5. The outgoing photon beam consists of the probe photons, survived after pair production ($\sim 10^5$), and a substantial amount of new born photons from radiation of produced pairs ($\sim 10^8$). The remaining probe photons are still confined within $\theta \le \theta_{\max}$ as the off-forward scattering ($\sim\alpha^2$) is negligible. After propagating through the laser field, the average polarization of probe photons changes to $\bar{\xi} = (-0.53, -0.60, 0.37)$ [Figs. 4(c)–4(e)], while the larger-angle photons exhibit a distinct linearly polarized: $\bar{\xi}' = (0, 0, 0.59)$ [Fig. 4(b)].

To analyze the simulation results, we use simplified estimations. The VD is described by Eq. (5). In the case of the photon initial polarization $\xi_1 \approx 1$ and $\xi_3 \approx 0$, the VD

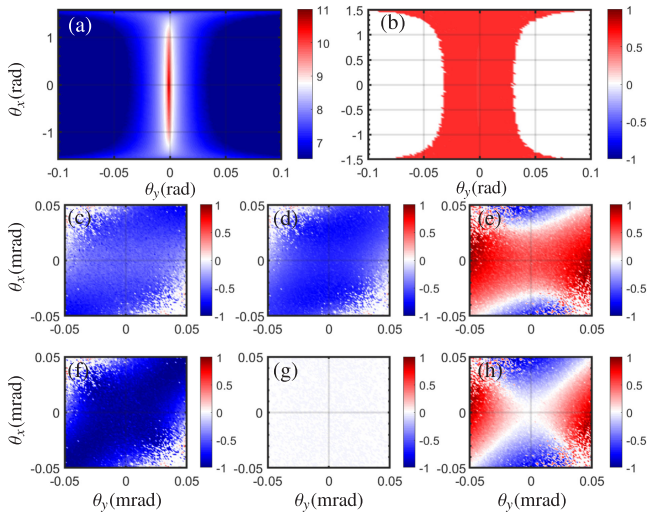

FIG. 4. Top row: the photon angular distribution after the interaction: (a) for the density $d^2N_\gamma/d\theta_x d\theta_y$ and (b) for the photon polarization ξ_3, with $\theta_{x,y}$ in mrad. Middle row: the angular distribution of photon polarization within $|\theta_{x,y}| \in [0, \theta_{\max}]$ for (c) degree of linear polarization at $\pm 45°$ with respect to polarization basis $P_1^{\mathrm{LP}} = \xi_1$, (d) degree of circular polarization with $P^{\mathrm{CP}} = \xi_2$, and (e) degree of linear polarization along polarization basis with $P_3^{\mathrm{LP}} = \xi_3$. Bottom row: same as the middle row, but without VP effects.

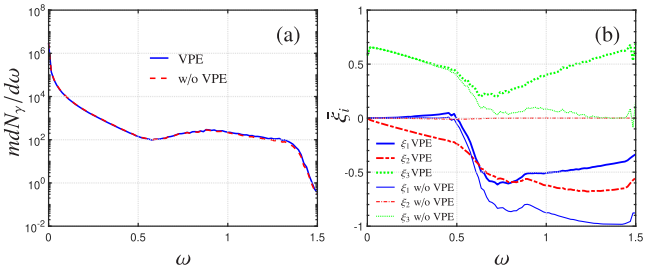

FIG. 5. (a) Photon spectra with (solid line) and without (red dashed line) VP effect (VPE). (b) The average photon polarization vs photon energy ω (GeV): ξ_1 (blue solid line), ξ_2 (red dot-dashed line), ξ_3 (green dotted line), with VP effect (thick line) and without VP effect (thin line).

acts as a polarization damper to reduce ξ_1 but to increase ξ_3. Meanwhile, the VB induces a polarization rotation from ξ_1 to ξ_2 according to Eq. (B10), resulting in a decrease of ξ_1 and an increase of ξ_2. With these equations, we estimate the average polarization for a 1 GeV photon after the interaction $\bar{\xi} = (-0.53, -0.65, 0.39)$, which is in a qualitative accordance with Figs. 4(c)–4(e).

In the highly nonlinear regime $\chi_\gamma \gtrsim 1$, considerable amounts of pairs are produced. The photons emitted by the generated electrons and positrons are mixed with probe photons that carry photonic signals of VP. To clarify the impact of secondary photons and reveal the pure VP effects, we artificially turn off the polarization variation during the no-pair production process. The average polarization of photons at small angle becomes $\bar{\xi}' = (-0.87, 0.0, 0.06)$; see Figs. 4(f)–4(h). The circular polarization ξ_2' disappears without VP regardless of photon emissions. However, the radiation of pairs affects the linearly polarized of final photons. The average polarization of the emitted photons by unpolarized electrons (positrons) we estimate using the result of Ref. [46],

$$\xi_1' = \xi_2' = 0, \xi_3' = \mathrm{K}_{\frac{2}{3}}(z_q)\left[\frac{\varepsilon^2+\varepsilon'^2}{\varepsilon'\varepsilon}\mathrm{K}_{\frac{2}{3}}(z_q) - \int_{z_q}^{\infty} dx \mathrm{K}_{\frac{1}{3}}(x)\right]^{-1}, \tag{7}$$

where $z_q = \frac{2}{3}\frac{\omega}{\chi_e \varepsilon'}$ with ε and ε' being the electron (positron) energy before and after emission, respectively. Since ξ_3' is inversely proportional to the emitted photon energy ω', the average polarization at a small angle is reduced by $\sim 1\%$ because of the mixing of the emitted hard photons. For soft photon emissions in the large angle region [Fig. 4(b)], we have $\xi_1' = \xi_2' = 0$ and $\xi_3' \approx 0.5$ according to Eq. (7), resulting in an average polarization of the entire beam as $\bar{\xi} = (0.0, 0.0, 0.59)$. In the high-energy regime, photon emission of produced pairs significantly broadens the angular distribution [Figs. 4(a) and 4(b)] and changes the average polarization of detected photons. Therefore, accounting for the photon emissions is necessary for accurately distinguishing the VP effect.

The full spectrum including all photons is shown in Fig. 5. The spectrum and polarization exhibit distinct behavior in the two regions divided by $\omega_c = 0.6$ GeV. The density distribution in the low-energy region has a feature of synchrotron radiation as it mostly consists of emitted photons, while the high-energy region exhibits a flat-top structure just as for the probe photons [Fig. 5(a)]. We find an increase of $\xi_{2,3}$ and decrease of ξ_1 in the high-energy region due to VP [Fig. 5(b)] because the polarization of probe photons is significantly affected by VB and VD. Interestingly, the photons emitted in the low-energy region also present a sizeable circular polarization ξ_2, indicating that the created e^+e^- pairs obtain longitudinal polarization when taking into account VP.

The polarization features of the created positrons are shown in Fig. 6. The positrons are longitudinally polarized with average polarization of $\sim 13\%$ and highest polarization up to $\sim 70\%$ [Figs. 6(b) and 6(f)]. The yield of positrons is $N_{e^+e^-} \approx 7.5 \times 10^5 \sim 0.75 N_\gamma$ [Figs. 6(a) and 6(e)]. In the high-energy region, most of the probe photons are converted to pairs via nonlinear Breit-Wheeler process. The longitudinal polarization of positrons stems from the helicity transfer of circular polarization from the probe photons, that is induced by VB at the early stage of interaction. The emitted photons, detrimental to the high-precision measurement of photonic signals, have a

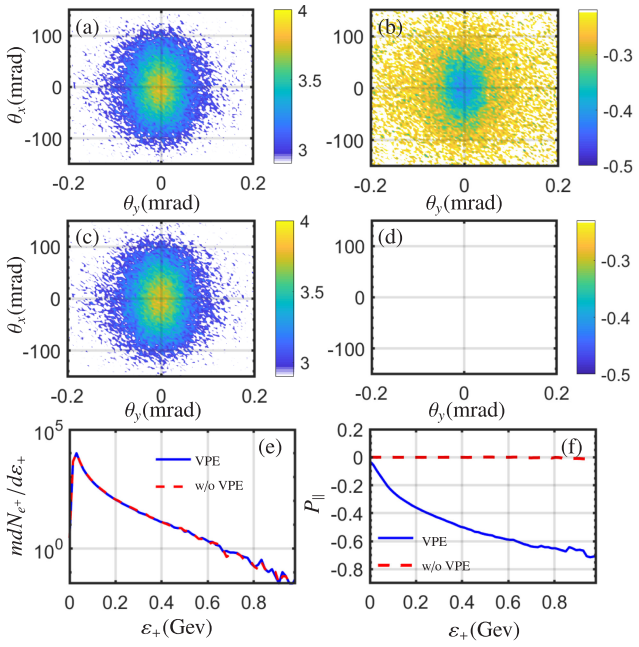

FIG. 6. Top row: the positron angular distribution: (a) for the number density $d^2N_{e^+}/d\theta_x d\theta_y$ (mrad^{-2}) and (b) for the longitudinal polarization $P_\parallel$, when $\theta_{x,y}$ are in mrad. Middle row: same as top row but without VP effects. Bottom row: (e) positron number density $mdN_{e^+}/d\varepsilon_+$ and (f) the longitudinal polarization vs positron energy ε_+ (GeV), with (blue solid line) VP and without (red dashed line) the VP effect.

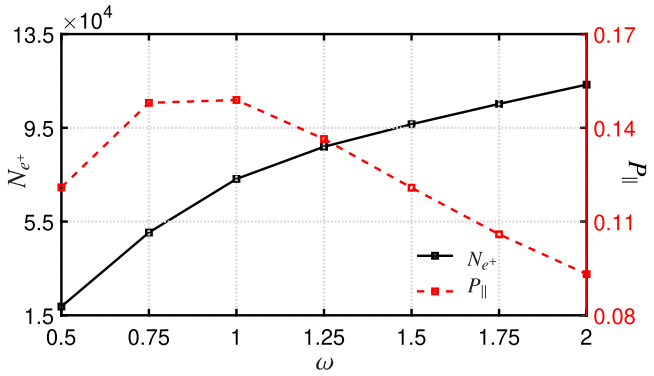

FIG. 7. The scaling law of positron number N_{e^+} (black solid line) and longitudinal polarization $P_\parallel$ (red dashed line) vs energy of probe photon ω (GeV). The probe photons' number is $N_\gamma = 1 \times 10^5$, and $\xi = (1, 0, 0)$. The laser parameters are the same as in Figs. 4–6.

negligible impact on the fermionic signal, as secondary pair production from soft radiation is minimal ($\sim 10^{-2} N_{e^+e^-}$). Thus, the emergence of longitudinal polarization is essentially a pure signature of VB. As can be seen from Fig. 6(d), the longitudinal polarization vanished without VP.

For experimental feasibility, we estimated the impact of probe photons energy on fermionic signals of VB; see Fig. 7. As the energy of the probe photon increases, the strength of VB signal also increases due to the larger χ_γ, because the high photon energy could accelerate the rotation from ξ_1 to ξ_2 for a fixed laser duration. Therefore, the longitudinal polarization of positrons increases with photons energy within some limits, before reaching $\sim 15\%$ at $\omega = 0.75$ GeV in the case of parameters of Fig. 7. Afterward, the polarization saturates within some photon energy range and further decreases with higher ω. This is because with higher ω, and higher χ_γ, the probe photon undergoes pair production before attaining a significant circular polarization due to VB. As a result, unlike the scaling law of positron density that monotonously increases with photon energy, the polarization purity has an optimal energy range within the interval of $\omega/\mathrm{GeV} \in [0.75, 1]$.

IV. EXPERIMENTAL FEASIBILITY OF A VACUUM POLARIZATION MEASUREMENT

A. Møller polarimetry for detecting positron polarization

Let us discuss the feasibility of VB detection taking advantage of the positron polarization. There are conventional techniques for measuring longitudinal polarization of positrons (electrons), such as Compton [55–57] and Møller polarimetries [58–60]. For the discussed parameter regime, the Møller polarimetry is more advantageous, which employs the scattering of polarized solid targets off the positrons (electrons) off a solid targets. Here, the longitudinal polarization is deduced via the measured asymmetry $\langle R \rangle = \frac{N_+ - N_-}{N_+ + N_-}$, where $N_\pm$ are the number of scattered positrons when the positron helicity is parallel or antiparallel to the target polarization [59]. The cross section in the center of the momentum frame of the electron reads

$$\frac{d\sigma}{d\Omega'} = \frac{d\sigma_0}{d\Omega'}\left(1 + \sum_{i,j} P^i_B A_{i,j} P^j_T\right), \tag{8}$$

where $P^i_B (P^j_T)$ are the components of the beam (target) polarization, as measured in the rest frame of the beam (target) positrons. Here, we set a new coordinate system with z' axis along the momentum of the positron beam and the y' axis normal to the Møller scattering plane. The prime in the positron coordinate definition is for distinguishing it from that used for the laser-electron interaction.

The cross section is characterized by the unpolarized cross section $\frac{d\sigma_0}{d\Omega'}$ and nine asymmetries $A_{i,j}$. The beam polarization components P^i_B are extracted from the measurement of the spin-dependent cross section on a target of known polarization P_T and using Eq. (8). To lowest order in QED, the unpolarized cross section and nine asymmetries are the following in the ultrarelativistic approximation [59]:

$$\begin{aligned}
\frac{d\sigma_0}{d\Omega'} &= \left[\frac{\alpha(1+\cos\theta'_{\mathrm{CM}})(3+\cos^2\theta'_{\mathrm{CM}})}{2m\sin^2\theta'_{\mathrm{CM}}}\right]^2, \\
A_{z'z'} &= -\frac{(7+\cos^2\theta'_{\mathrm{CM}})\sin^2\theta'_{CM}}{(3+\cos^2\theta'_{\mathrm{CM}})^2}, \\
-A_{x'x'} &= A_{y'y'} = \frac{\sin^4\theta'_{\mathrm{CM}}}{(3+\cos^2\theta'_{\mathrm{CM}})^2}, \\
A_{x'z'} &= A_{z'x'} = -\frac{2\sin^3\theta'_{\mathrm{CM}}\cos\theta'_{\mathrm{CM}}}{\gamma(3+\cos^2\theta'_{\mathrm{CM}})^2}, \\
A_{x'y'} &= A_{y'x'} = A_{y'z'} = A_{z'y'} = 0.
\end{aligned} \tag{9}$$

Note that θ'_{CM} is the center of mass (CM) scattering angle. To measure the longitudinal polarization, the experimentally determined quantity is the asymmetry parameter

$$R = \frac{N_+ - N_-}{N_+ + N_-}. \tag{10}$$

Considering the connection between the laboratory scattering angle and the center of mass scattering angle,

$$\begin{aligned}
\theta'^2_{\mathrm{L}} &= 2m_e\left(\frac{1}{p_s} - \frac{1}{p_i}\right), \\
p_s &= \frac{p_i}{2}(1+\cos\theta'_{\mathrm{CM}}),
\end{aligned} \tag{11}$$

the $A_{z'z'}$ is a function of the incident electron energy γ and the detection angle θ'_d in the laboratory frame. Here, p_s (p_i) is the momentum of the scattered (incident) positrons for Møller scattering.

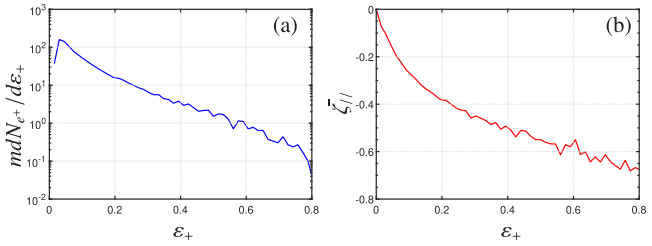

FIG. 8. (a) Positron density and (b) longitudinal polarization within 10 mrad.

In our setup, the positrons after the interaction are distributed in a wide angle range of $\Delta\theta_x \sim 200$ mrad. We collect the positrons within 10 mrad for the measurement of vacuum birefringence. The spectrum and polarization distribution for positrons within 10 mrad are shown in Fig. 8. It can be seen that the positrons have a quite large energy range $\Delta\varepsilon \sim \varepsilon_0$ around the mean energy ε_0. Then, we have to take into account that the rest frames of the particles are different at different energies. In this case, the asymmetry parameter for a certain detection angle θ'_d is given by

$$\langle R\rangle = \frac{N_+ - N_-}{N_+ + N_-} = \frac{\sum_i \sigma_{0i}\zeta_i^z A'_{zzi} P_T^z N_{e_i^+} n_z l}{\sum_i \sigma_{0i} N_{e_i^+} n_z l} = \frac{\sum_i \sigma_{0i}\zeta_i^z A'_{zzi} N_{e_i^+}}{\sum_i \sigma_{0i} N_{e_i^+}} P_T^z, \tag{12}$$

where $\sigma_{0i} \approx \frac{d\sigma_{0i}}{d\Omega}\Delta\Omega'$ is the unpolarized cross section for positrons with energy ε_i^+ and $\Delta\Omega'$ is related to the detection angle in the laboratory frame via $\Delta\Omega' = -\frac{8mp_i\theta'_L}{(2m+p_i\theta'^2_L)^2}\Delta\theta'_L$. n_z and l are the density and length of the target, and $N_{e_i^+}$ is the number of positrons with energy ε_i^+, respectively. The maximum target polarization is $P_T^z = 8.52\%$. The maximum of asymmetry is $\langle R\rangle_{\max} \approx 0.0089$ for $\theta'_L = 0.1414$ rad [Fig. 9]. The current experimental capability of measuring the asymmetry parameter is $A_m = 0.5\% \times P_T \times \frac{7}{9} = 3.89 \times 10^{-3} P_T \ll \langle R\rangle_{\max} = 0.1 \times P_T$.

Next, we estimate the measurement time for vacuum birefringence with 5σ confidence level. The thin foil circular disks used in the Møller polarimeter are a few microns thick (13–25 μm), which should be smaller than the milliradiation length (mRL $= 10^{-3}$ radiation length) to avoid secondary photon emissions. Consider a target composed of a Fe-Vo alloy (Supermendur: 49% Fe, 49% Co, 2%Va by mass). A 25 μm foil is only 1.5 mRL, which can be used in a Møller polarimeter. The density of the target is 8.12 g/cm^3 [density near room temperature (g/cm^3): Fe 7.874, Co 8.9, Ni 8.902]. The electron density of the target can be calculated from $n_z = \rho N_A \langle Z\rangle/\langle A\rangle \approx 2.26 \times 10^{24}$ where $\langle Z\rangle$ and $\langle A\rangle$ are the average atomic number and mass number of the Vacoflux alloy, $N_A = 6.022 \times 10^{23}$ is Avogadro's number, and ρ is the density of the foil. The average atomic number $\langle Z\rangle$ is 26.43 (Fe 26, Co 27, Va 23), and average the mass number is 57 a.u. (Fe 55.8 a.u., Co 58.9 a.u., Va 50.94 a.u.).

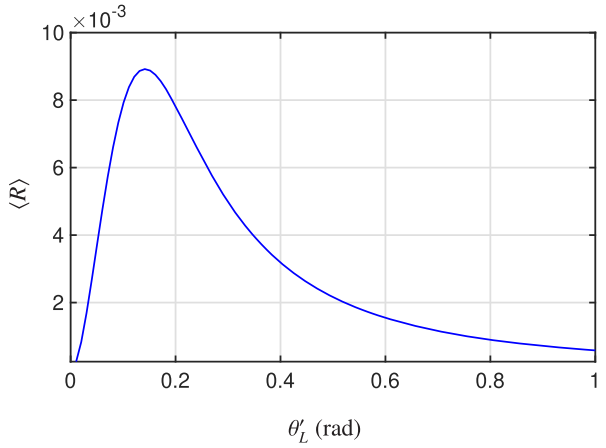

FIG. 9. The scaling law of asymmetry $\langle R\rangle$ vs detection angle θ'_L in the laboratory frame.

The standard deviation then can be estimated with

$$\Delta R = \frac{1}{\sqrt{N_+ + N_-}} = \frac{1}{\sqrt{\sum_i \sigma_{0i}(\theta'_L = 0.14) N_{e_i^+} n_z l}}. \tag{13}$$

For the detecting angle of $\theta'_L = 0.14$ rad with $\Delta\theta'_L = 0.03$ rad, the standard deviation is $\Delta R = 0.0236$. To achieve a confidence level of $\langle R\rangle = 5\Delta R$, one needs $\tilde{N}_{e^+} = 2.35 \times 10^8$ positrons. Assuming electron bunches with $N^0_{e^-} = 1 \times 10^8$ is used for Compton backscattering, our scheme could generate $N_{e^+} = 1.3 \times 10^6$ positrons within 10 mrad. Using a few PW laser with a repetition rate of 1/60 Hz [53,61], the measurement of vacuum birefringence with 5σ confidence level requires a measurement time of $\tilde{N}_{e^+}/N_e/(1/60)/3600 \approx 3$ h. The measurement time can be further reduced if all outgoing positrons are focused to a small angle and included in the measurement.

Achieving a 5σ confidence level for fermionic signals requires 180 shots of a 10 PW laser. For a laser with a repetition rate of 1/60 Hz, it requires 3 h in a continuous measurement. In real experiments, the measurement is still feasible but with an extended measurement time to maintain the quality of each laser shot. For instance, in the 10 PW beamline at the Shanghai Superintense Ultrafast Laser Facility, completing 180 shots usually takes approximately 2 months [62]. Meanwhile, the measurement time can be reduced at the expense of confidence level. A measurement time of 7 min is implied for a measurement with σ confidence level.

The estimation of the Müller polarimetry signal is given in Appendix D.

B. Impact of secondary photon emissions

The impact of secondary emissions on the photonic signal are shown in Figs. 11(a) and 11(b). The emissions of pairs extend the spectrum to the low-energy region [Fig. 11(a)] and significantly affect the average polarization around 0.5 GeV [Fig. 11(b)]. The emitted photons are linearly polarized with $\bar{\xi}_3 \approx 59\%$; see Fig. 11(a). Fortunately, the polarization and spectrum in the high-energy region are not affected by the radiation of pairs. If the γ photons with energy higher than 0.75 GeV are postselected, a clean signal of vacuum polarization can be obtained. Otherwise, the low-energy photons will overwhelm the VP photonic signal.

The impact of secondary emissions on the fermionic signal is shown in Figs. 11(c) and 11(d). The radiation of pairs results in a redistribution of positron energy; see Figs. 11(c) and 11(d). Without radiation, the positrons exhibit a wide energy distribution, extending up to 1.5 GeV. However, when radiation reaction is included, the energy distribution of the positrons peaks at 30 MeV. Moreover, the secondary emission alters the distribution of polarization. The maximum polarization increases from 34% to 71% when taking into account secondary emissions. This can be explained as follows. Without radiation, positrons with different polarizations are mixed, resulting in a relatively low average polarization [see Fig. 10(c)]. The positrons at larger θ_y have smaller longitudinal polarization [Fig. 10(c)] but higher transverse polarization [Figs. 10(a) and 10(b)], and vice versa at smaller θ_y. While positrons with polarization levels of up to 70% already exist, they are overwhelmed by the large number of positrons with lower polarization. When radiation is taken into account, the positrons with different polarization are separated due to the spin-dependent radiation probability, i.e., $dW_{\rm rad} \propto dW^0 - \frac{\omega}{\varepsilon_+}\zeta_y \mathrm{K}_{\frac{1}{3}}(z_q)$ with dW^0 being the unpolarized

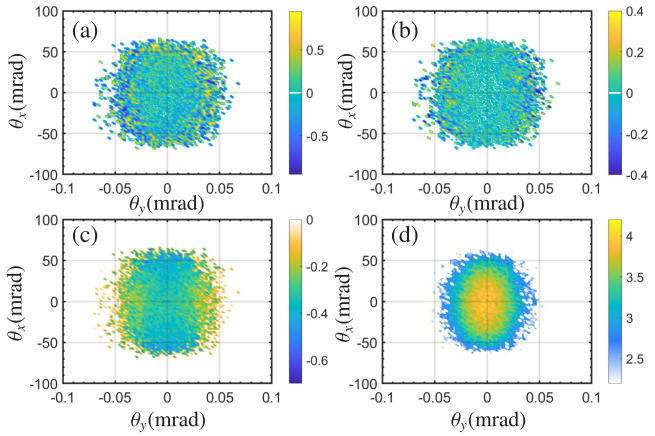

FIG. 10. The angular distribution of the polarization of positrons with $\varepsilon_+ > 1$ GeV: (a) for ζ_x, (b) for ζ_y, and (c) for ζ_z. (d) The angular distribution of the number density $d^2N/d\theta_x d\theta_y$ for positrons with $\varepsilon_+ > 1$ GeV.

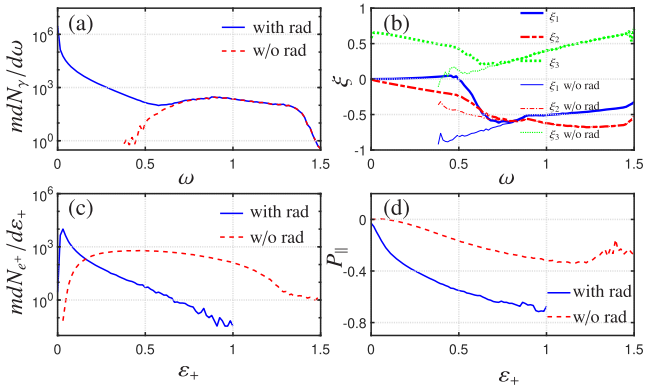

FIG. 11. (a) Photon spectrum $mdN_\gamma/d\omega$ with (blue solid line) and without (red dashed line) pair radiation. (b) The distribution of photon polarization vs photon energy ω (GeV) with (thick lines) and without (thin lines) radiation from pairs for: ξ_1 (blue solid line), ξ_2 (red dot-dashed line), and ξ_3 (green dotted line). (c) Positron spectrum $mdN_{e^+}/d\varepsilon_+$. (d) Longitudinal polarization of positrons $P_\parallel$ vs ε_+ (GeV) taking into account pair radiation (blue solid line) or neglecting it (red dashed line). The laser pulse duration $\tau_p = 50$ fs.

radiation probability. Specifically, positrons with large negative ζ_y (and correspondingly small ζ_z) undergo more dramatic radiation reactions and are therefore more significantly redshifted. As the components with low polarization are reduced, $\bar{\zeta}_z$ at the high-energy end of the spectrum increases [Fig. 11(d)].

Even though the maximum of polarization increases, the average polarization decreases from 17% to 13%. This is confirmed by the following equation describing the evolution of the average longitudinal polarization [63]:

$$\frac{dP_\parallel}{dt} = -\frac{e}{m}\boldsymbol{P}_\perp \cdot \left[\left(\frac{g}{2}-1\right)\beta \times \boldsymbol{B} + \left(\frac{g\beta}{2}-\frac{1}{\beta}\right)\boldsymbol{E}\right] - \frac{\alpha m}{\sqrt{3}\pi\gamma} P_\parallel \int_0^\infty \frac{u^2 du}{(1+u)^3 \int_{z_q}^\infty dx \mathrm{K}_{\frac{1}{3}}(x)} \approx -\frac{\alpha m}{\sqrt{3}\pi\gamma} P_\parallel \int_0^\infty \frac{u^2 du}{(1+u)^3 \int_{z_p}^\infty dx \mathrm{K}_{\frac{1}{3}}(x)}, \tag{14}$$

where $u = \omega'/\varepsilon'$ and the last term is due to radiation. The approximation in Eq. (14) is justified because $\boldsymbol{P}_\perp \cdot \boldsymbol{E} = 0$ for radiative polarization in linearly polarized laser fields. According to Eq. (14), the longitudinal polarization $|dP_\parallel|$ decreases due to radiation.

C. Impact of the initial γ beam parameters

1. Initial γ photons energy

We have employed the relatively low-energy electrons (LEPS2 beamline at SPring-8) because the photon energy obtained by perfect backscattering of 8.4 GeV electron is $\omega = (1+\beta)\varepsilon\omega_0/(\varepsilon - \varepsilon\beta + 2\omega_0) \approx 1.13$ GeV, which is

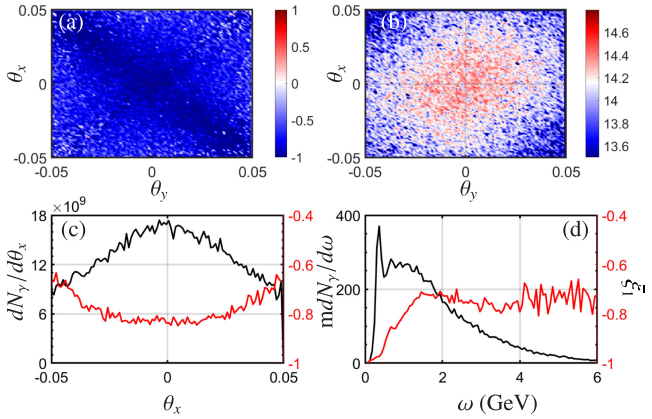

FIG. 12. (a) Angular distribution of γ photon density $\log_{10} d^2N/d\theta_x/d\theta_y$ (mrad^{-2}) and (b) polarization ξ_1 vs θ_x (mrad) and θ_y (mrad) obtained with parameters of LUXE: $a_0 = 3\sqrt{2}$, $\varepsilon_i = 17.5$ GeV, pulse duration 30 fs. (c) The angular distribution of γ photon density $dN_\gamma/d\theta_x$ (mrad^{-1}) (black solid line) and polarization ξ_1 (red solid line) vs θ_x. (d) The energy distribution of γ photon density $mdN_\gamma/d\omega$ (GeV^{-1}) (black solid line) and polarization ξ_1 (red solid line) vs ω(GeV).

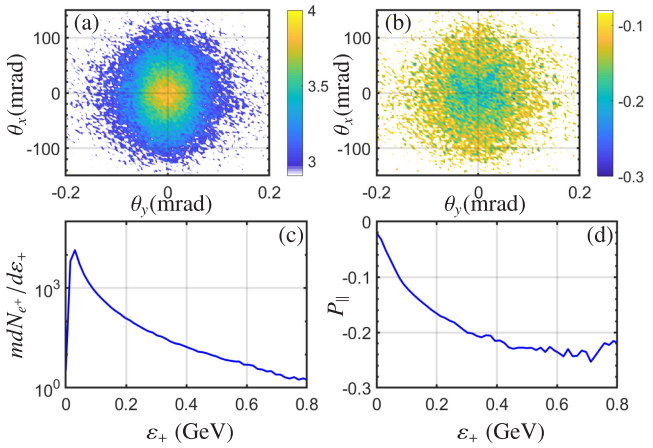

FIG. 13. The positron angular distribution produced by photons of Fig. 12: (a) for the number density $d^2N_{e^+}/d\theta_x d\theta_y$ (mrad^{-2}) and (b) for the longitudinal polarization $P_\parallel$, when $\theta_{x,y}$ are in mrad. (c) Positron number density $md N_{e^+}/d\varepsilon_+$ and (d) the longitudinal polarization vs positron energy ε_+ (GeV). $N_{\gamma 0} = 8 \times 10^5$.

within the optimal energy range for enhancing signal of vacuum polarization.

Can a better result be obtained with a more advanced electron source, e.g., LUXE? With the high-energy electrons at LUXE (17.5 GeV), the interaction enters the nonlinear nonperturbative regime, where the photon density and energy increase, however, at the expense of a decrease in polarization. The production rate of photons increases from $N_\gamma \approx 0.5 N_{e_0^-}$ to $N_\gamma \approx 0.66 N_{e_0^-}$ [Figs. 12(b) and 12(c)], while the average polarization of positrons decreases from $|\xi_1| = 0.91$ to $\xi_1 = 0.78$ [Fig. 12(a)]. Meanwhile, the photon spectrum undergoes broadening to 6 GeV [Fig. 12(d)]. Hence, the photons obtained under the parameters of the LUXE project fall outside the optimal range for conducting vacuum polarization measurements. For instance, with the probe γ photons obtained with 17.5 GeV electrons, the positrons number increases from $N_{e^+} = 3.8 \times 10^7$ to 8.2×10^7 for initial electrons $N_{e_0^-} = 10^8$ [Figs. 13(a) and 13(c)], while the longitudinal polarization of produced positrons decreases from 13% to 6.4% [Figs. 13(b) and 13(d)]. The substantial decreases in polarization leads to a longer measurement time, $t_{\text{meas}} = 6.7$ h.

2. Initial γ photon polarization

The variability in the collection angle of photons could introduce uncertainty to the polarization of the γ-ray beam. As the collision angle of the γ-ray beam increases from $\Delta\theta_{\max} = 0.05$ to 0.1 mrad, the photon yield increases while the average polarization decreases from $|\xi_1| = 0.9$ to 0.7. This decline in photon polarization results in an extended measurement time for vacuum polarization. However, this is counterbalanced by the enhanced positron yield. Consequently, the measurement time increases slightly from 2.9 to 3 h as the polarization degree decreases; see Fig. 14(a).

D. Impact of the laser parameters

1. Pulse duration

The duration of the laser pulse controls the conversion of the circularly polarized γ photons into the longitudinally polarized positrons and determines the balance between the photonic and fermionic signals of VP.

The effect of VP is less significant in a shorter laser pulse with a pulse duration of $\tau_p = 25$ fs, compared to the 50 fs case discussed so far; cf. Fig. 15 with Fig. 16. However, the number of survived outgoing photons is larger. Thus, in the considered scenario, half of the probe photons decay into pairs, while the other half survive without undergoing pair production. For an initial count of $N^0_{e^-} = 1 \times 10^8$ electrons, we are left with $N_\gamma = 2.5 \times 10^7$ probe photons available for measuring vacuum polarization. Even though the photon yield is higher compared to the $\tau_p = 50$ fs case [Fig. 15(a); cf. Fig. 16(a)], the variation in polarization induced by vacuum polarization is smaller, due to the reduced interaction length [Fig. 15(b); cf. Fig. 16(b)]. The average photon polarization in the small-angle region ($\theta < 0.05$ mrad) becomes $\xi = (78\%, 37\%, 21\%)$. In this case, employing the polarimetry method outlined in Sec. IV B, a single-shot measurement could achieve a confidence level of 3σ for vacuum birefringence and 6σ for vacuum dichroism.

Meanwhile, as the pulse duration decreases from 50 to 25 fs, the positron yield reduces from $N_{e^+e^-} = 7.5 \times 10^7$ to

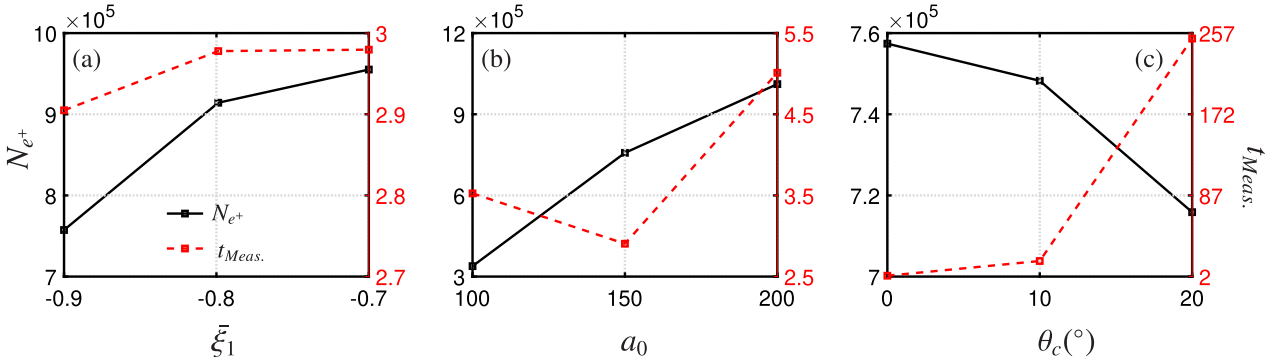

FIG. 14. The scaling laws of positron yield N_e^+ (black solid line) and meaurement time t_{Meas} in unit of hours (red dashed line) vs (a) the polarization of the initial γ photons $\bar{\xi}_1$, (b) laser intensity a_0, and (c) the collision angle θ_c between laser and the γ-ray beam.

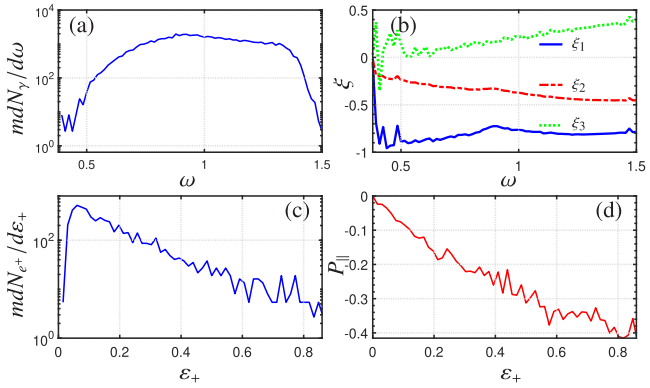

FIG. 15. (a) Photon density $mdN_\gamma/d\omega$ and (b) polarization distribution within 0.05 mrad vs photon energy ω (GeV) for: ξ_1 (blue solid line), ξ_2 (red dot-dashed line), and ξ_3 (green dotted line). (c) Positron density $mdN_{e^+}/d\varepsilon_+$ and (d) the distribution of longitudinal polarization within 10 mrad vs positron energy ε_+ (GeV). The laser pulse duration $\tau = 25$ fs.

$N_{e^+e^-} = 2.5 \times 10^7$ [Fig. 15(c)]. The fermionic signal also becomes less pronounced. The average longitudinal polarization of positrons decreases to $P_\parallel = 8\%$, with the maximum polarization reaching $P_\parallel^m = 40\%$ [Fig. 15(d)]. In this scenario, to achieve a confidence level of 5σ for measuring vacuum birefringence, the required measurement time would need to be extended to 7 h. When the pulse duration is reduced, the effects of vacuum polarization remain detectable, but achieving a reasonable confidence level necessitates a relatively longer measurement time.

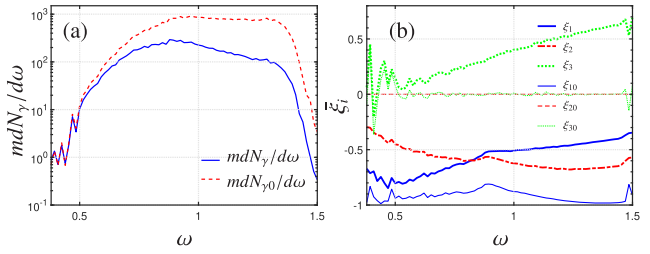

FIG. 16. (a) Density of probe γ photons before (red dashed line) and after (blue solid line) interacting with the laser. (b) Polarization of probe γ photons before (thin line) and after (thick line) interacting with the laser. The laser pulse duration is $\tau_p = 50$ fs.

2. Laser intensity

We examine the fermionic signal with a laser intensity of $a_0 = 50$, which is comparable with current laser parameters at ELI Beamlines (1 PW pulses, repetition rate 10 Hz, pulse duration 30 fs). Assume the probe γ photons are obtained by linear Compton scattering of a linearly polarized laser pulse off a 15 GeV electron beam. The generated γ photons within 0.02 mrad are highly polarized with $\xi_1 = -0.87$ and have an average energy of $\omega_\gamma = 3$ GeV, with the energy spread $\Delta\omega_\gamma/\omega_\gamma = 0.54$; see Fig. 17. The yield of the γ photons within 0.02 mrad is $N_\gamma = 0.44 N_{e_0^-}$. Next, the probe photons propagate through a 1 PW laser pulse ($a_0 = 50$).

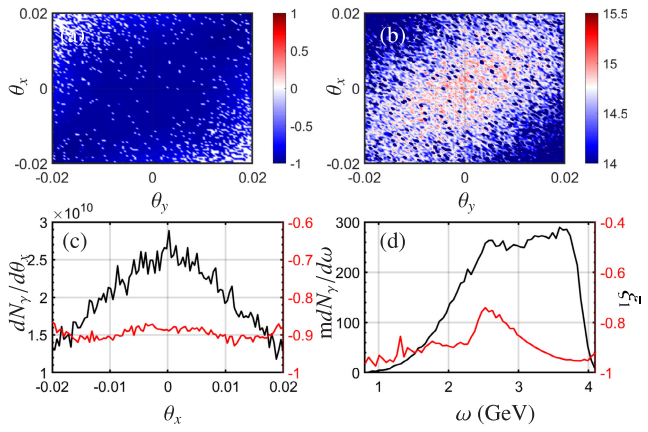

FIG. 17. (a) Angular distribution of γ-photon density $\log_{10} d^2N/d\theta_x/d\theta_y$ (mrad^{-2}) and (b) polarization ξ_1 vs θ_x (mrad) and θ_y (mrad). (c) The angular distribution of γ photon density $dN_\gamma/d\theta_x$ (mrad^{-1}) (black solid line) and polarization ξ_1 (red solid line) vs θ_x. (d) The energy distribution of γ photon density $mdN_\gamma/d\omega$ (GeV^{-1}) (black solid line) and polarization ξ_1 (red solid line) vs ω(GeV). The initial electron energy is 15 GeV.

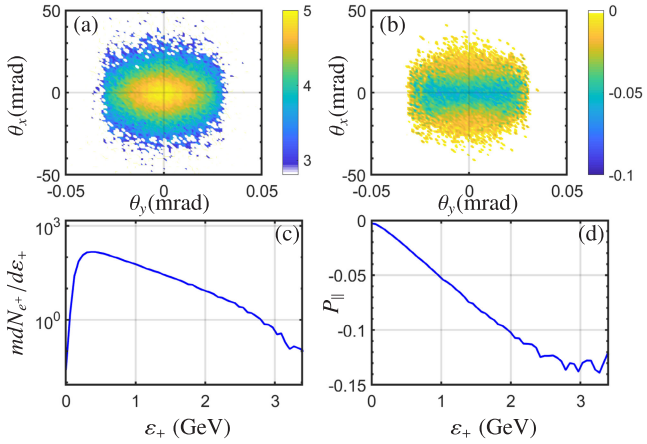

FIG. 18. Top row: the positron angular distribution: (a) for the number density $d^2N_{e^+}/d\theta_x d\theta_y$ (mrad^{-2}) and (b) for the longitudinal polarization $P_\parallel$, when $\theta_{x,y}$ are in mrad. Bottom row: (c) positron number density $mdN_{e^+}/d\varepsilon_+$ and (d) the longitudinal polarization vs positron energy ε_+ (GeV). Laser intensity $a_0 = 50$ and pulse duration $t_p = 10T$.

The polarization features of the created positrons are shown in Fig. 18. The positrons are longitudinally polarized with average polarization of 3.8% and highest polarization up to ∼14% [Figs. 18(b) and 18(f)]. The yield of positrons is $N_{e^+e^-} \approx 2.4 \times 10^5 \sim 0.25N_\gamma$ [Figs. 18(a) and 18(e)]. Despite the decrease in total pair yield, the number of pairs within 10 mrad increases from $N_{e^+e^-} = 1.3 \times 10^6$ to 7.3×10^6 due to the smaller deflection angle. The increase in positron density at small angles is beneficial for polarization measurement but is offset by the decrease in polarization. In order to detect VB at the 5σ confidence level, the required positron number is $\tilde{N}_{e^+} = 1.4 \times 10^9$, corresponding to 200 shorts of measurement. Considering the high repetition rate of the 1 PW laser is 10 Hz, the measurement time is 20 sec, much smaller than the 10 PW case.

The scaling law of measurement time and laser intensity is shown in Fig. 14(b). With the increase of the laser intensity, the positron density increases monotonously, while the measurement time has an optimal at $a_0 = 150$ [Fig. 14(b)]. When the laser intensity increases from 100 to 150, the measurement time decreases from 3.5 to 2.9 h due to the larger χ_γ. However, further increases in laser intensity lead to an increase in measurement time, as the probe photon undergoes pair production before attaining significant circular polarization.

3. Collision angle of γ and laser beams

The collision angle could also affect the pair yield and consequently induce a increase of measurement time. As shown in Fig. 14(c), the pairs yield decreases slightly from $N_{e^+e^-} = 7.6 \times 10^5$ to $N_{e^+e^-} = 7.2 \times 10^5$ with the increase of collision angle from $\theta_c = 0°$ to $\theta_c = 20°$. When the positrons within 10 mrad are collected for measurement, t_{Meas} increases significantly from 2.9 to 257 h. However, if the detection angle of positrons is rotated with collision angle, the measurement time remains ∼3 h, which is robust against the fluctuation of θ_c.

V. CONCLUSION

Concluding, we analyzed a setup for a high-energy VP measurement using a 10 PW laser system with 1 GeV linearly polarized γ probe photons, with a newly developed complete QED Monte Carlo simulation method for describing vacuum polarization in the high-energy limit. Deviating from the conventional photonic signal of VP, we identified the fermionic signal of VB in the positron polarization that is free from disturbances caused by secondary emissions and more feasible for VB detection. In our scheme, previously avoided real pairs are employed as a better source for detecting VB, providing a novel method for probing quantum vacuum nonlinearity.The fermionic signal remains robust against experimental fluctuations, enabling a 5σ confidence level within a few hours.

In addition, the high polarization and density of γ photons allows for a single-shot measurement for vacuum polarization, achieving an 8σ confidence level. The revealed polarization feature of positrons provides an alternative way of measuring vacuum birefringence. As a byproduct, our scheme supplies a well-collimated (∼0.05 mrad), dense ($\sim 2.7 \times 10^5$), and highly circularly polarized γ-ray beam with an average polarization reaching up to 60% as well as dense (7.5×10^5) longitudinally polarized positrons with a highest polarization of ∼70% via QED loop effects. Besides the potential application in detecting vacuum birefringence, such polarized particles are highly demanded in studies of fundamental physics and related applications, in particular, in nuclear physics, astrophysics, and high-precision high-energy physics at accelerators, including parity violation, photon-photon scattering, and photoproduction of mesons.

ACKNOWLEDGMENTS

We gratefully acknowledge helpful discussions with Professor Y.-F. Li. This work is supported by the National Natural Science Foundation of China (Grant No. 12074262) and the National Key R&D Program of China (Grant No. 2021YFA1601700).

APPENDIX A: THE QED TREATMENT OF VACUUM POLARIZATION

According to the QED loop calculation in Ref. [34], the $O(\alpha^0)$-order loop contribution is

$$P^0 = \frac{1}{2}(1 + \boldsymbol{\xi}_i \cdot \boldsymbol{\xi}'), \tag{A1}$$

where the initial and final photon polarizations are represented by the Stokes parameters $\boldsymbol{\xi}_i$ and $\boldsymbol{\xi}'$, respectively. The $O(\alpha)$-order loop contribution via the interference diagram in Fig. 2(b) reads

$$P^1 = \langle P^L \rangle + P_0^L \cdot n_0 + P_1^L \cdot n_1 + n_1 \cdot P_{10}^L \cdot n_0. \tag{A2}$$

The sum of these contributions is

$$P^L = P_{VD}^L + P_{VB}^L \tag{A3}$$

$$\begin{aligned} P_{VD}^L = \frac{1}{2}\Bigg(1 - \int_0^\omega d\varepsilon C_p \Bigg[\int_{z_p}^\infty dx \mathrm{K}_{\frac{1}{3}}(x) + \frac{\varepsilon^2+\varepsilon_+^2}{\varepsilon_+\varepsilon}\mathrm{K}_{\frac{2}{3}}(u') \\ - \mathrm{K}_{\frac{2}{3}}(z_p)\hat{\mathbf{e}}_{\mathbf{3}}\cdot\boldsymbol{\xi}_i\Bigg]\Bigg) + \frac{1}{2}\boldsymbol{\xi}'\Bigg[\Bigg(1 - \int_0^\omega d\varepsilon C_p \\ \times \Bigg[\int_{z_p}^\infty dx \mathrm{K}_{\frac{1}{3}}(x) + \frac{\varepsilon^2+\varepsilon_+^2}{\varepsilon_+\varepsilon}\mathrm{K}_{\frac{2}{3}}(z_p)\Bigg]\Bigg)\boldsymbol{\xi}_i \\ + \int_0^\omega d\varepsilon C_p \mathrm{K}_{\frac{2}{3}}(z_p)\hat{\mathbf{e}}_{\mathbf{3}}\Bigg], \end{aligned} \tag{A4}$$

$$\begin{aligned} P_{VB}^L &= \frac{\alpha m^2}{2\omega^2}\Delta t \int d\varepsilon \frac{\mathrm{Gi}'(\rho)}{\rho}\boldsymbol{\xi}'\cdot\varepsilon_{3ij}\cdot\boldsymbol{\xi}_i \\ &= \frac{\alpha m^2}{2\omega^2}\Delta t \int d\varepsilon \frac{\mathrm{Gi}'(\rho)}{\rho}(\xi_1'\xi_{i2} - \xi_2'\xi_{i1}), \end{aligned} \tag{A5}$$

where $C_p = \frac{\alpha m^2}{\sqrt{3}\pi\omega^2}$; $z_p = \frac{2}{3\chi_\gamma}\frac{\omega^2}{\varepsilon_+\varepsilon}$; $\chi_\gamma = |F_{\mu\nu}k^\nu|/mF_{cr}$ is the strong-field quantum parameter; ε_+ and ε are the energy of produced positrons and electrons, respectively; $\rho = \frac{1}{[\delta(1-\delta)\chi_\gamma]^{2/3}}$; $\delta = \varepsilon/\omega$; and $\mathrm{Gi}'(x)$ is the Scorer prime function.

The first term of Eq. (A3) P_{VD}^L, stemming from the imaginary part of of the polarization operator, describes VD, while the second term P_{VB}^L is associated with the real part of the polarization operator and induces VB.

When the pair production is negligible, the loop probability of all orders can be resummed into a time-ordered exponential [34]:

$$\begin{aligned} P &= \frac{1}{2}\boldsymbol{\xi}'\cdot e^{-4\langle P^{BW}\rangle}[(\epsilon_0\epsilon_0+\epsilon_3\epsilon_3)\cosh\nu + (\epsilon_0\epsilon_3+\epsilon_3\epsilon_0)\sinh\nu \\ &\quad + (\epsilon_1\epsilon_1+\epsilon_2\epsilon_2)\cos\varphi + (\epsilon_1\epsilon_2-\epsilon_2\epsilon_1)\sin\varphi]\boldsymbol{\xi}_i \\ &= \frac{e^{-W_P}}{2}[(\cosh v + \xi_{i3}\sinh v) + \xi_1'(\xi_{i1}\cos\varphi + \xi_{i2}\sin\varphi) \\ &\quad + \xi_2'(-\xi_{i1}\sin\varphi + \xi_{i2}\cos\varphi) + \xi_3'(\sinh v + \xi_{i3}\cosh v)], \end{aligned} \tag{A6}$$

where $W_P = 4\langle P^{BW}\rangle$ is the total pair production probability, and

$$\varphi = \frac{\alpha m^2}{\omega^2}\Delta t \int d\varepsilon \frac{\mathrm{Gi}'(\rho)}{\rho}, \qquad v = -\frac{\alpha m^2}{\omega^2}\Delta t \int d\varepsilon \frac{\mathrm{Ai}'(\rho)}{\rho}, \tag{A7}$$

with $\mathrm{Ai}'(x)$ being the Airy prime function. The final Stokes parameters for the remaining probe photons read

$$\begin{aligned} \xi_1^f &= \frac{\xi_1\cos\varphi + \xi_2\sin\varphi}{\cosh v + \xi_3\sinh v}, \\ \xi_2^f &= \frac{-\xi_1\sin\varphi + \xi_2\cos\varphi}{\cosh v + \xi_3\sinh v}, \\ \xi_3^f &= \frac{\sinh v + \xi_3\cosh v}{\cosh v + \xi_3\sinh v}. \end{aligned} \tag{A8}$$

The photon number at a distance l takes the form

$$N(l) = e^{-W_P}(\cosh v + \xi_3\sinh v)N(0). \tag{A9}$$

Equations (A8) and (A9) coincide with Eq. (15.20) given in Ref. [64]. The average polarization of a photon ensemble defined as $\bar{\xi}^f = \xi_L^f W^L$, with the final polarization state of photons $\xi_L^f = (\xi_1^f, \xi_2^f, \xi_3^f)$ and the loop probability $W^L = e^{-W_P}(\cosh v + \xi_3\sinh v)$, reads

$$\begin{pmatrix} \bar{\xi}_0 \\ \bar{\xi}_1 \\ \bar{\xi}_2 \\ \bar{\xi}_3 \end{pmatrix} = e^{-W_P}\begin{pmatrix} \cosh\nu & 0 & 0 & \sinh\nu \\ 0 & \cos\varphi & \sin\varphi & 0 \\ 0 & -\sin\varphi & \cos\varphi & 0 \\ \sinh\nu & 0 & 0 & \cosh\nu \end{pmatrix}\begin{pmatrix} \xi_0 \\ \xi_1 \\ \xi_2 \\ \xi_3 \end{pmatrix}, \tag{A10}$$

which coincides with Eq. (11) of Ref. [28]. However, rather than averaging over the survived ones as in the present work, the polarization defined in Ref. [28] is obtained by averaging over the initial photon number:

$$\bar{\xi}^f = \xi_L^f W^L = \frac{N_\uparrow^{NP} - N_\downarrow^{NP}}{N_\uparrow^{NP} + N_\downarrow^{NP}}\cdot\frac{N^{NP}}{N^{NP}+N^P} = \frac{N_\uparrow^{NP} - N_\downarrow^{NP}}{N^{NP}+N^P}, \tag{A11}$$

where $N^{NP} = N_\uparrow^{NP} + N_\downarrow^{NP}$ is the number of photons that are survived from pair production, with $N_\uparrow^{NP}$ and $N_\downarrow^{NP}$ being the number of photons with final polarization $\boldsymbol{\xi}' = \pm\boldsymbol{\xi}^f$ and $\boldsymbol{\xi}^f = (\xi_1^f, \xi_2^f, \xi_3^f)/\sqrt{\xi_1^{f2} + \xi_2^{f2} + \xi_3^{f2}}$, and N^P is the number of photons that decay into pairs. Therefore, the average polarization defined by Eq. (A11) is by the factor $\frac{N^{NP}}{N^{NP}+N^P}$ smaller than the polarization of the survived photons in the final state. For small $\chi_\gamma \ll 1$, the difference between the definitions of the photon final polarization is negligible.

APPENDIX B: MONTE CARLO SIMULATION METHOD FOR VACUUM BIREFRINGENCE AND DICHROISM

In this section, we present the spin- and polarization-resolved Monte Carlo method for the tree process (nonlinear Breit-Wheeler) and the loop process (vacuum polarization). In our Monte Carlo code, at each simulation step Δt, the pair production is determined by the total pair production probability, and the positron energy and polarization are determined by the spin-resolved spectral probability [48], using the common algorithms [40–47]. If the pair production event is rejected, the photon polarization state is determined by the photon-polarization dependent loop probability w^{NP}.

1. Spin- and polarization-resolved pair production probability

The pair production probability including all the polarization and spin characteristics takes the form [47,48]

$$\begin{aligned} dW^P(\boldsymbol{\xi},\boldsymbol{\zeta}_-,\boldsymbol{\zeta}_+) &= \frac{1}{2}(dW_{11}+dW_{22})+\frac{\xi_1}{2}(dW_{21}+dW_{12}) \\ &\quad -i\frac{\xi_2}{2}(dW_{21}-dW_{12})+\frac{\xi_3}{2}(dW_{11}-dW_{22}) \\ &= \frac{1}{2}(G_0+\xi_1 G_1+\xi_2 G_2+\xi_3 G_3), \end{aligned} \tag{B1}$$

where

$$\begin{aligned} G_0 &= \frac{C_p}{2}d\varepsilon\Bigg\{\Bigg\{\int_{z_p}^{\infty}dx\mathrm{K}_{\frac{1}{3}}(x)+\frac{\varepsilon_+^2+\varepsilon^2}{\varepsilon_+\varepsilon}\mathrm{K}_{\frac{2}{3}}(z_p)\Bigg\} \\ &\quad +\Bigg\{\int_{z_p}^{\infty}dx\mathrm{K}_{\frac{1}{3}}(x)-2\mathrm{K}_{\frac{2}{3}}(z_p)\Bigg\}(\boldsymbol{\zeta}_-\cdot\boldsymbol{\zeta}_+) \\ &\quad +\left[\frac{\omega}{\varepsilon_+}(\boldsymbol{\zeta}_+\cdot\mathbf{b})-\frac{\omega}{\varepsilon}(\boldsymbol{\zeta}_-\cdot\mathbf{b})\right]\mathrm{K}_{\frac{1}{3}}(z_p) \\ &\quad +\Bigg\{\frac{\varepsilon_+^2+\varepsilon^2}{\varepsilon\varepsilon_+}\int_{z_p}^{\infty}dx\mathrm{K}_{\frac{1}{3}}(x) \\ &\quad -\frac{(\varepsilon_+-\varepsilon)^2}{\varepsilon\varepsilon_+}\mathrm{K}_{\frac{2}{3}}(z_p)\Bigg\}(\boldsymbol{\zeta}_-\cdot\hat{\mathbf{v}})(\boldsymbol{\zeta}_+\cdot\hat{\mathbf{v}})\Bigg\}, \end{aligned}$$

$$\begin{aligned} G_1 &= \frac{C_p}{2}d\varepsilon\Bigg\{-\frac{\varepsilon_+^2-\varepsilon^2}{2\varepsilon_+\varepsilon}\mathrm{K}_{\frac{2}{3}}(z_p)\hat{\mathbf{v}}\cdot[\boldsymbol{\zeta}_+\times\boldsymbol{\zeta}_-] \\ &\quad +\left[\frac{\omega}{\varepsilon}(\boldsymbol{\zeta}_+\cdot\mathbf{s})-\frac{\omega}{\varepsilon_+}(\boldsymbol{\zeta}_-\cdot\mathbf{s})\right]\mathrm{K}_{\frac{1}{3}}(z_p) \\ &\quad -\frac{\omega^2}{2\varepsilon_+\varepsilon}\int_{z_p}^{\infty}dx\mathrm{K}_{\frac{1}{3}}(x)\{(\boldsymbol{\zeta}_-\cdot\mathbf{b})(\boldsymbol{\zeta}_+\cdot\mathbf{s}) \\ &\quad +(\boldsymbol{\zeta}_-\cdot\mathbf{s})(\boldsymbol{\zeta}_+\cdot\mathbf{b})\}\Bigg\}, \end{aligned}$$

$$\begin{aligned} G_2 &= \frac{C_p}{2}d\varepsilon\Bigg\{-\frac{\omega^2}{2\varepsilon_+\varepsilon}\mathrm{K}_{\frac{1}{3}}(z_p)[\mathbf{s}\cdot(\boldsymbol{\zeta}_-\times\boldsymbol{\zeta}_+)] \\ &\quad +\left(\frac{\omega}{\varepsilon_+}\int_{z_p}^{\infty}dx\mathrm{K}_{\frac{1}{3}}(x)+\frac{\varepsilon_+^2-\varepsilon^2}{\varepsilon_+\varepsilon}\mathrm{K}_{\frac{2}{3}}(z_p)\right)(\boldsymbol{\zeta}_+\cdot\hat{\mathbf{v}}) \\ &\quad +\left(\frac{\omega}{\varepsilon}\int_{z_p}^{\infty}dx\mathrm{K}_{\frac{1}{3}}(x)-\frac{\varepsilon_+^2-\varepsilon^2}{\varepsilon_+\varepsilon}\mathrm{K}_{\frac{2}{3}}(z_p)\right)(\boldsymbol{\zeta}_-\cdot\hat{\mathbf{v}}) \\ &\quad -\frac{\varepsilon_+^2-\varepsilon^2}{2\varepsilon_+\varepsilon}\mathrm{K}_{\frac{1}{3}}(z_p)[(\boldsymbol{\zeta}_-\cdot\hat{\mathbf{v}})(\boldsymbol{\zeta}_+\cdot\mathbf{b})+(\boldsymbol{\zeta}_-\cdot\mathbf{b})(\boldsymbol{\zeta}_+\cdot\hat{\mathbf{v}})]\Bigg\}, \end{aligned}$$

$$\begin{aligned} G_3 &= \frac{C_p}{2}d\varepsilon\Bigg\{-\mathrm{K}_{\frac{2}{3}}(z_p)+\frac{\varepsilon_+^2+\varepsilon^2}{2\varepsilon_+\varepsilon}\mathrm{K}_{\frac{2}{3}}(z_p)(\boldsymbol{\zeta}_-\cdot\boldsymbol{\zeta}_+) \\ &\quad +\left[-\frac{\omega}{\varepsilon}(\boldsymbol{\zeta}_+\cdot\mathbf{b})+\frac{\omega}{\varepsilon_+}(\boldsymbol{\zeta}_-\cdot\mathbf{b})\right]\mathrm{K}_{\frac{1}{3}}(z_p) \\ &\quad -\frac{(\varepsilon_+-\varepsilon)^2}{2\varepsilon_+\varepsilon}\mathrm{K}_{\frac{2}{3}}(z_p)(\boldsymbol{\zeta}_-\cdot\hat{\mathbf{v}})(\boldsymbol{\zeta}_+\cdot\hat{\mathbf{v}}) \\ &\quad +\frac{\omega^2}{2\varepsilon_+\varepsilon}\int_{z_p}^{\infty}dx\mathrm{K}_{\frac{1}{3}}(x)[(\boldsymbol{\zeta}_-\cdot\mathbf{b})(\boldsymbol{\zeta}_+\cdot\mathbf{b}) \\ &\quad -(\boldsymbol{\zeta}_-\cdot\mathbf{s})(\boldsymbol{\zeta}_+\cdot\mathbf{s})]\Bigg\}. \end{aligned} \tag{B2}$$

Here, $\hat{\mathbf{v}}$ is the unit vector along velocity of the produced electron, $\mathbf{s}$ the unit vector along the transverse component of electron acceleration, and $\mathbf{b}=\hat{\mathbf{v}}\times\mathbf{s}$. The 3-vector $\boldsymbol{\xi}=(\xi_1,\xi_2,\xi_3)$ is the Stokes parameter of the incoming photon, ω is the photon energy, and ε_+ and ε_- are the energy of the created positron and electron, respectively.

a. Spin quantization axis for the produced electron

After taking the sum over positron polarizations [48],

$$d\tilde{W}^p(\boldsymbol{\xi},\boldsymbol{\zeta}_-)=\frac{1}{2}(\tilde{G}_0+\xi_1\tilde{G}_1+\xi_2\tilde{G}_2+\xi_3\tilde{G}_3),$$

$$\begin{aligned} \tilde{G}_0 &= C_p d\varepsilon\Bigg\{\int_{z_p}^{\infty}dx\mathrm{K}_{\frac{1}{3}}(x)+\frac{\varepsilon_+^2+\varepsilon^2}{\varepsilon_+\varepsilon}\mathrm{K}_{\frac{2}{3}}(z_p) \\ &\quad -\frac{\omega}{\varepsilon}(\boldsymbol{\zeta}_-\cdot\mathbf{b})\mathrm{K}_{\frac{1}{3}}(z_p)\Bigg\} \end{aligned}$$

$$\tilde{G}_3 = C_p d\varepsilon\left\{-\mathrm{K}_{\frac{2}{3}}(z_p)+\frac{\omega}{\varepsilon_+}(\boldsymbol{\zeta}_-\cdot\mathbf{b})\mathrm{K}_{\frac{1}{3}}(z_p)\right\}$$

$$\tilde{G}_1 = -C_p d\varepsilon\frac{\omega}{\varepsilon_+}(\boldsymbol{\zeta}_-\cdot\mathbf{s})\mathrm{K}_{\frac{1}{3}}(z_p)$$

$$\tilde{G}_2 = C_p d\varepsilon\left\{\left(\frac{\omega}{\varepsilon}\int_{z_p}^{\infty}dx\mathrm{K}_{\frac{1}{3}}(x)-\frac{\varepsilon_+^2-\varepsilon^2}{\varepsilon_+\varepsilon}\mathrm{K}_{\frac{2}{3}}(z_p)\right)(\boldsymbol{\zeta}_-\cdot\hat{\mathbf{v}})\right\}, \tag{B3}$$

which can be rewritten in the form [48]

$$d\tilde{W}^p(\boldsymbol{\xi},\boldsymbol{\zeta}_-)=\frac{1}{2}(a_-+\boldsymbol{\zeta}_-\cdot\boldsymbol{b}_-)$$
$$a_-=C_p d\varepsilon\left[\int_{z_p}^{\infty}dx\mathrm{K}_{\frac{1}{3}}(x)+\frac{\varepsilon_+^2+\varepsilon^2}{\varepsilon_+\varepsilon}\mathrm{K}_{\frac{2}{3}}(z_p)-\xi_3\mathrm{K}_{\frac{2}{3}}(z_p)\right]$$
$$\boldsymbol{b}_-=-C_p d\varepsilon\left\{\xi_1\frac{\omega}{\varepsilon_+}\mathbf{s}\mathrm{K}_{\frac{1}{3}}(z_p)+\left(\frac{\omega}{\varepsilon}-\xi_3\frac{\omega}{\varepsilon_+}\right)\mathbf{b}\mathrm{K}_{\frac{1}{3}}(z_p)+\left[-\frac{\omega}{\varepsilon}\int_{z_p}^{\infty}dx\mathrm{K}_{\frac{1}{3}}(x)+\frac{\varepsilon_+^2-\varepsilon^2}{\varepsilon_+\varepsilon}\mathrm{K}_{\frac{2}{3}}(z_p)\right]\xi_2\hat{\mathbf{v}}\right\}. \tag{B4}$$

The final polarization vector of the produced electron resulting from the scattering process itself is $\boldsymbol{\zeta}_f^-=\frac{\boldsymbol{b}_-}{a_-}$, which determines the spin quantization axis for the produced electron $\boldsymbol{\zeta}_f^-$: $\boldsymbol{n}^-=\boldsymbol{\zeta}_f^-/|\boldsymbol{\zeta}_f^-|$.

b. Spin quantization axis for the produced positron

After taking the sum over electron polarizations, we obtain [48]

$$d\bar{W}^p(\boldsymbol{\xi},\boldsymbol{\zeta}_+)=\frac{1}{2}(\bar{G}_0+\xi_1\bar{G}_1+\xi_2\bar{G}_2+\xi_3\bar{G}_3),$$
$$\bar{G}_0=C_p d\varepsilon\left\{\int_{z_p}^{\infty}dx\mathrm{K}_{\frac{1}{3}}(x)+\frac{\varepsilon_+^2+\varepsilon^2}{\varepsilon_+\varepsilon}\mathrm{K}_{\frac{2}{3}}(z_p)+\frac{\omega}{\varepsilon_+}(\boldsymbol{\zeta}_+\cdot\mathbf{b})\mathrm{K}_{\frac{1}{3}}(z_p)\right\}$$
$$\bar{G}_3=C_p d\varepsilon\left\{-\mathrm{K}_{\frac{2}{3}}(z_p)-\frac{\omega}{\varepsilon}(\boldsymbol{\zeta}_+\cdot\mathbf{b})\mathrm{K}_{\frac{1}{3}}(z_p)\right\}$$
$$\bar{G}_1=C_p d\varepsilon\frac{\omega}{\varepsilon}(\boldsymbol{\zeta}_+\cdot\mathbf{s})\mathrm{K}_{\frac{1}{3}}(z_p)$$
$$\bar{G}_2=C_p d\varepsilon\left\{\left(\frac{\omega}{\varepsilon_+}\int_{z_p}^{\infty}dx\mathrm{K}_{\frac{1}{3}}(x)+\frac{\varepsilon_+^2-\varepsilon^2}{\varepsilon_+\varepsilon}\mathrm{K}_{\frac{2}{3}}(z_p)\right)(\boldsymbol{\zeta}_+\cdot\hat{\mathbf{v}})\right\}, \tag{B5}$$

which can also be written as [48]

$$d\bar{W}^p(\boldsymbol{\xi},\boldsymbol{\zeta}_+)=\frac{1}{2}(a_++\boldsymbol{\zeta}_+\cdot\boldsymbol{b}_+)$$
$$a_+=C_p d\varepsilon\left[\int_{z_p}^{\infty}dx\mathrm{K}_{\frac{1}{3}}(x)+\frac{\varepsilon_+^2+\varepsilon^2}{\varepsilon_+\varepsilon}\mathrm{K}_{\frac{2}{3}}(z_p)-\xi_3\mathrm{K}_{\frac{2}{3}}(z_p)\right] \tag{B6}$$
$$\boldsymbol{b}_+=C_p d\varepsilon\left\{\xi_1\mathrm{K}_{\frac{1}{3}}(z_p)\frac{\omega}{\varepsilon}\mathbf{s}+\left(\frac{\omega}{\varepsilon_+}-\xi_3\bar{C}_0 d\varepsilon\frac{\omega}{\varepsilon}\right)\mathbf{b}\mathrm{K}_{\frac{1}{3}}(z_p)+\xi_2\hat{\mathbf{v}}\left(\frac{\omega}{\varepsilon_+}\int_{z_p}^{\infty}dx\mathrm{K}_{\frac{1}{3}}(x)+\frac{\varepsilon_+^2-\varepsilon^2}{\varepsilon_+\varepsilon}\mathrm{K}_{\frac{2}{3}}(z_p)\right)\right\}. \tag{B7}$$

The final polarization vector of the produced positron resulting from the scattering process itself is $\boldsymbol{\zeta}_f^+=\frac{\boldsymbol{b}_+}{a_+}$, which determines the spin quantization axis for the produced positron: $\boldsymbol{n}^+=\boldsymbol{\zeta}_f^+/|\boldsymbol{\zeta}_f^+|$.

After taking the sum over positron and electron polarizations, we get the spin unresolved pair production probability:

$$dW_T^P(\boldsymbol{\xi})=a_+. \tag{B8}$$

2. Polarization-resolved no-pair production probability

If a pair production event is rejected, the photon polarization should also change due to the dependency of the no-pair production probability on the photon polarization:

$$W^{NP}(\boldsymbol{\xi},\boldsymbol{\xi}')=\frac{1}{2}(c^{NP}+\boldsymbol{d}^{NP}\cdot\boldsymbol{\xi}')$$
$$c^{NP}=1-\int_0^{\omega}a_+d\varepsilon\Delta t$$
$$\boldsymbol{d}^{NP}=\boldsymbol{\xi}\left(1-\int_0^{\omega}d\varepsilon C_p\left[\int_{z_p}^{\infty}dx\mathrm{K}_{\frac{1}{3}}(x)+\frac{\varepsilon_+^2+\varepsilon^2}{\varepsilon\varepsilon_+}\mathrm{K}_{\frac{2}{3}}(z_p)\right]\Delta t\right)+\int_0^{\omega}d\varepsilon C_p\hat{\mathbf{e}}_{\mathbf{3}}\mathrm{K}_{\frac{2}{3}}(z_p)\Delta t, \tag{B9}$$

where $\hat{\mathbf{e}}_{\mathbf{3}}=(0,0,1)$. The final polarization state of the photon after the no-pair-production step becomes $\boldsymbol{\xi}_f^{NP}=\boldsymbol{d}^{NP}/c^{NP}$, which defines a quantization axis for photon polarization: $\boldsymbol{n}^{NP}=\boldsymbol{\xi}_f^{NP}/|\boldsymbol{\xi}_f^{NP}|$.

3. Algorithm of event generation

(1) *Update photon polarization*: At each time step, the photon polarization needs to be updated with local acceleration.
   (a) Calculate the instantaneous polarization basis vectors $\mathbf{e}_1=\mathbf{s}-(\mathbf{n}\cdot\mathbf{s})\mathbf{n}$ and $\mathbf{e}_2=\mathbf{n}\times\mathbf{s}$, with unit vectors of electron acceleration $\mathbf{s}$ and photon propagation direction $\mathbf{n}$.

(b) Update the photon Stokes parameters

$$\xi_1' = \xi_1 \cos(2\psi) - \xi_3 \sin(2\psi),$$
$$\xi_2' = \xi_2,$$
$$\xi_3' = \xi_1 \sin(2\psi) + \xi_3 \cos(2\psi),$$

where ψ is the angle between the new and old basis vectors.

(2) *Decide pair production event*: At each simulation step, the pair production and the electron (positron) energy are determined by the probability of Eq. (B8) with the updated Stokes parameters, using the common stochastic procedure.
   (a) Generate two random numbers $r_1, r_2 \in [0,1]$ with uniform probability.
   (b) Compute the pair production probability $P(r_1) = dW_T^P(\boldsymbol{\xi}, r_1\omega)\Delta t$ for the given initial photon polarization $\boldsymbol{\xi}$, electron energy $\varepsilon = r_1\omega$, and positron energy $\varepsilon_+ = (1-r_1)\omega$.
   (c) If $r_2 < P(r_1)$, an e^+e^- pair is created. Otherwise, reject.

(3) *Decide the polarization of outgoing particles*:
   (a) Case 1: $P(r_1) > r_2$: pair production occurs. After each pair production, the spin of the produced electron (positron) is either parallel or antiparallel to $\boldsymbol{n}^-$ ($\boldsymbol{n}^+$) using the stochastic procedure with another random number $r_3 \in [0,1]$. With the given ε_-, ε_+ and photon polarization $\boldsymbol{\xi}$, compute the pair production probability $P_{\zeta_-\zeta_+} = dW^P(\boldsymbol{\xi}, \boldsymbol{\zeta}_-, \boldsymbol{\zeta}_+)\Delta t$ with $\{\boldsymbol{\zeta}_-, \boldsymbol{\zeta}_+\} \in \{\uparrow, \downarrow\}$ indicating parallel or antiparallel with respective quantization axis.
      (i) If $r_3 < P_{\downarrow\downarrow}$, the electron is spin down with respect to $\boldsymbol{n}^-$ and the positron is spin down with respect to $\boldsymbol{n}^+$, i.e., $\boldsymbol{\zeta}_- = -\boldsymbol{n}^-$, $\boldsymbol{\zeta}_+ = -\boldsymbol{n}^+$.
      (ii) If $P_{\downarrow\downarrow} < r_3 < P_{\downarrow\downarrow} + P_{\downarrow\uparrow}$, $\boldsymbol{\zeta}_- = -\boldsymbol{n}^-$ and $\boldsymbol{\zeta}_+ = \boldsymbol{n}^+$.
      (iii) If $P_{\downarrow\downarrow} + P_{\downarrow\uparrow} < r_3 < P_{\downarrow\downarrow} + P_{\downarrow\uparrow} + P_{\uparrow\downarrow}$, $\boldsymbol{\zeta}_- = \boldsymbol{n}^-$ and $\boldsymbol{\zeta}_+ = -\boldsymbol{n}^+$.
      (iv) If $P_{\downarrow\downarrow}+P_{\downarrow\uparrow}+P_{\uparrow\downarrow} < r_3 < P_{\downarrow\downarrow}+P_{\downarrow\uparrow}+P_{\uparrow\downarrow}+P_{\uparrow\uparrow}$, $\boldsymbol{\zeta}_- = \boldsymbol{n}^-$ and $\boldsymbol{\zeta}_+ = \boldsymbol{n}^+$.
   (b) Case 2: $P(r_1) < r_2$: pair production is rejected. The photon polarization state collapses into one of its basis states defined with respect to $\boldsymbol{n}^{NP}$.
      (i) Generate another random number $r_4 \in [0,1]$.
      (ii) Compute the no-pair-production probability $P_{\xi'} = W^{NP}(\boldsymbol{\xi}, \boldsymbol{\xi}')$ for a given initial photon polarization $\boldsymbol{\xi}$. Here, $\boldsymbol{\xi}' \in \{\uparrow, \downarrow\}$ indicates spin parallel or antiparallel with $\boldsymbol{n}^{NP}$.
      (iii) If $P_\uparrow/(P_\uparrow + P_\downarrow) > r_4$, $\boldsymbol{\xi}' = \boldsymbol{n}^{NP}$. Otherwise, $\boldsymbol{\xi}' = -\boldsymbol{n}^{NP}$.

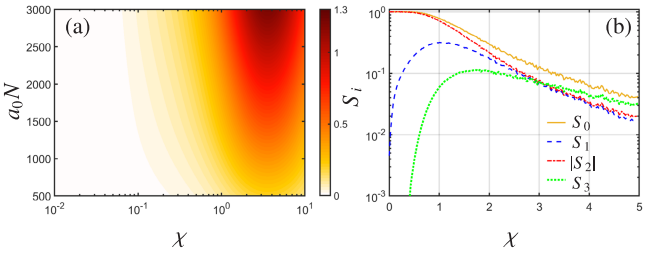

FIG. 19. (a) Plot of $\delta\phi$ as a function of χ and a_0N for a rectangular pulse profile. (b) Final Stokes parameters for γ photons propagating through the 10 PW laser pulse in the Extreme Light Infrastructure-Nuclear Physics [54] ($S^{(0)} = 1, 0, -1, 0$). The Stokes parameters are obtained by averaging over the probe photon number.

In the above algorithm, the pair spin (photon polarization) is determined by the spin-resolved (photon-polarization-resolved) probabilities according to the stochastic algorithm and instantaneously collapses into one of its basis states defined with respect to the instantaneous quantization axis. Alternatively, one could set the pairs in a mixed spin state $\boldsymbol{\zeta}'_\pm = \boldsymbol{\zeta}_f^\pm$ or photon polarization $\boldsymbol{\xi} = \boldsymbol{\xi}_f^{NP}$ in the case of no-pair production.

(4) *Rotate the photon polarization*: Calculate the instantaneous retarded phase induced by vacuum birefringence use Eq. (A7), and update ξ_1 and ξ_2 following Refs. [22,28,34]:

$$\begin{pmatrix} \xi_1^f \\ \xi_2^f \end{pmatrix} = \begin{pmatrix} \cos\varphi & \sin\varphi \\ -\sin\varphi & \cos\varphi \end{pmatrix} \begin{pmatrix} \xi_1 \\ \xi_2 \end{pmatrix}. \tag{B10}$$

4. Benchmark of our simulation method

We have demonstrated the no-pair-production probability used in our code corresponds to the loop probability, with which Eq. (15.20) in Ref. [64] and Eq. (11) in Ref. [28] can be reproduced. To further benchmark the accuracy of our code, we have plotted the phase variation induced by vacuum birefringence and final Stokes parameters for different parameters. With the parameters used in Ref. [28], our results are in good agreement with Figs. 4 and 5 in Ref. [28]; see Fig. 19.

APPENDIX C: ESTIMATE OF THE PHOTON YIELD IN THE COMPTON PROCESS

The yield of photons can be estimated using the perturbative QED theory for linear Compton scattering [3]. The total cross section for photons scatted by angles $\varphi \in [0, 2\pi]$ and $\theta \in [0, \theta_{\max}]$ is

$$\sigma_{bs} = \frac{4\pi r_e^2}{m^2 x^2} \int_0^{\theta_{\max}} \omega_\gamma^2 F_0 \sin\theta, \tag{C1}$$

where $r_e = \alpha/m = 2.818 \times 10^{-13}$ cm with m being the electron mass and

$$\begin{aligned} F_0 &= V + U^2 + 2U, \\ V &= x/y + y/x, U = 2/x - 2/y, \\ x &= \frac{2pk_0}{m^2} = \frac{2\varepsilon\omega_0}{m^2}(1+\beta), \\ y &= \frac{2pk'}{m^2} = \frac{2\varepsilon\omega_\gamma}{m^2}(1-\beta\cos\theta), \end{aligned} \tag{C2}$$

$\beta = |\vec{p}|/\varepsilon_0$ with $\varepsilon_0 = 8.4$ GeV being initial electron energy, $\vec{p}$ being the electron momentum, and $\omega_0 = 1.55$ eV being the energy of laser photon for linear Compton scattering. The energy ω_γ of the final photon is determined via 4-momentum conservation and is given by

$$\omega_\gamma = \frac{(1+\beta)\varepsilon\omega_0}{\varepsilon + \omega_0 - (\varepsilon\beta - \omega_0)\cos\theta}. \tag{C3}$$

For $\theta_{\max} = 0.05$ mrad, we have $\sigma_{bs} \approx 2.68 r_e^2$. Employing pulse duration $\Delta t = 10$ ps, $I = 4.3 \times 10^{16}$ W/cm^2, $\omega_0 = 1.55$ eV, one could estimate the yield of γ photons via $N_\gamma/N_e = \sigma_{bs}(I/\omega_0)\Delta t \approx 0.4$, which roughly coincides with our simulation results.

APPENDIX D: MÜLLER POLARIMETRY FOR DETECTING PHOTON POLARIZATION

When measuring vacuum birefringence via photonic signals, previous approaches employed small χ_γ or short interaction length to mitigate background noise stemming from real pair production. Consequently, the acquired ellipticity by probe photons was typically too small for detection. However, our method utilizes larger χ_γ, leading to the remaining probe photons acquiring substantial circular polarization. This significant enhancement enables the measurement of vacuum polarization using photonic signals. Note, however, that the pair production in this regime significantly suppresses the number of survived photons, having impact on the accuracy of the measurement. Even though the γ-ray polarimetry for circular polarization poses challenges, the decrease of ξ_1 and increase of ξ_3 can be regarded as the photonic signals for detecting VB and VD, respectively. The polarization of γ photons can also be detected by converting photons to electron and positron pairs in a high Z target. The asymmetry of the angular distribution of produced pairs can be used as photonic signals of vacuum birefringence and dichroism [28].

The cross section of electron-positron photoproduction by a photon with energy $\omega \ll m$ colliding with an atom (charge number Z) is given by [28,65]

$$d\sigma_{pp} = \frac{d\varphi}{2\pi}\{\sigma_0 S_0 + \sigma_1[S_1 \sin 2\varphi + S_3 \cos 2\varphi]\}, \tag{D1}$$

where

$$\begin{aligned} \sigma_0 &= 2\frac{Z^2\alpha r_e^2}{\omega^3}\int_m^{\omega-m} d\varepsilon \int_{m^2/\varepsilon^2}^1 d\zeta\{(\varepsilon^2+\varepsilon'^2)(3+2\Gamma) \\ &\quad + 2\varepsilon\varepsilon'[1+4u^2\zeta^2\Gamma]\}, \\ \sigma_1 &= 2\frac{Z^2\alpha r_e^2}{\omega^3}\int_m^{\omega-m} d\varepsilon \int_{m^2/\varepsilon^2}^1 d\zeta\{8\varepsilon\varepsilon' u^2\zeta^2\Gamma\}, \\ \Gamma &= \ln(1/\delta_i) - 2 - f(Z) + F(\delta/\zeta), \\ \zeta &= 1/(1+\vec{u}^2), \\ \vec{u} &= \vec{p}_\perp/m = |p_\perp|(\cos\varphi, \sin\varphi), \\ \delta &= m\omega/(2\varepsilon\varepsilon'), \\ f(Z) &= (Z\alpha)^2 \sum_{n=1}^{\infty} \frac{1}{n(n^2+(Z\alpha)^2)}, \\ F(\delta/\zeta) &= -\frac{1}{2}\sum_{i=1}^{3}\alpha_i^2 \ln(1+B_i) \\ &\quad + \sum_{i,j=1,i\neq j}^{3}\alpha_i\alpha_j\left[\frac{1+B_j}{B_i - B_j}\ln(1+B_j) + \frac{1}{2}\right], \\ B_i &= (\beta_i\zeta/\delta)^2, \beta_i = (Z^{1/3}/121)b_i, \\ \alpha_1 &= 0.1, \alpha_2 = 0.55, \alpha_3 = 0.35; \\ b_1 &= 6, b_2 = 1.2, b_3 = 0.3. \end{aligned}$$

For photons with a wide spectrum [see Fig. 16(a)], the asymmetries for detecting vacuum birefringence (R_B) and vacuum dichroism (R_D) are

$$\begin{aligned} R_B &= \frac{(N_{\pi/4} + N_{5\pi/4}) - (N_{3\pi/4} + N_{7\pi/4})}{(N_{\pi/4} + N_{5\pi/4}) + (N_{3\pi/4} + N_{7\pi/4})}, \\ R_D &= \frac{(N_0 + N_\pi) - (N_{\pi/2} + N_{3\pi/2})}{(N_0 + N_\pi) + (N_{\pi/2} + N_{3\pi/2})}, \end{aligned} \tag{D2}$$

where N_{β_0} denotes the number of pairs detected in the azimuthal angle range $\varphi \in (\beta_0 - \beta, \beta_0 + \beta)$ of the transverse plane, with $\beta = 33°$ as optimal angle for both observables, and

$$
\begin{aligned}
N_{\pi/4} = N_{5\pi/4} &= \sum_i N_{\gamma i} n_z l \int_{\pi/4-\beta}^{\pi/4+\beta} \frac{d\varphi}{2\pi} \{\sigma_{0i} S_{0i} \\
&\quad + \sigma_{1i}[S_{1i} \sin 2\varphi + S_{3i} \cos 2\varphi]\} \\
&= \sum_i N_{\gamma i} n_z l \left[\sigma_{0i} S_{0i} \frac{\beta}{\pi} + \sigma_{1i} S_{1i} \frac{\sin 2\beta}{2\pi}\right], \\
N_{3\pi/4} = N_{7\pi/4} &= \sum_i N_{\gamma i} n_z l \left[\sigma_{0i} S_{0i} \frac{\beta}{\pi} - \sigma_{1i} S_{1i} \frac{\sin 2\beta}{2\pi}\right], \\
N_0 = N_\pi &= \sum_i N_{\gamma i} n_z l \left[\sigma_{0i} S_{0i} \frac{\beta}{\pi} + \sigma_{1i} S_{3i} \frac{\sin 2\beta}{2\pi}\right], \\
N_{\pi/2} = N_{3\pi/2} &= \sum_i N_{\gamma i} n_z l \left[\sigma_{0i} S_{0i} \frac{\beta}{\pi} - \sigma_{1i} S_{3i} \frac{\sin 2\beta}{2\pi}\right].
\end{aligned} \tag{D3}
$$

Here, the subscript i denotes the variables for photons with energy of ω_i. Substituting the above expressions of N_{β_0} into Eq. (D2), we have

$$
\begin{aligned}
R_B &= \frac{\sum_i N_{\gamma i} \sigma_{1i} S_{1i} \sin(2\beta)}{\sum_i N_{\gamma i} \sigma_{0i} S_{0i} 2\beta}, \\
R_D &= \frac{\sum_i N_{\gamma i} \sigma_{1i} S_{3i} \sin(2\beta)}{\sum_i N_{\gamma i} \sigma_{0i} S_{0i} 2\beta}.
\end{aligned} \tag{D4}
$$

Using a effective thickness of 3.66×10^{20} corresponding to a conversion efficiency of $\eta = 0.01$ with $\sigma_0 = 344 r_e^2$ in Ref. [28] and the polarization distribution of photon after interaction with the laser [see Fig. 6(a)], we obtained the asymmetry $R_B = -0.0369$ and $R_D = 0.0246$. In the case in which the photons do not interact with the laser, we obtain $R_B^0 = -0.0617$ and $R_D^0 = 0$. The observables of vacuum polarization are $\mathcal{A}_B = R_B - R_B^0 = 0.0247$ and $\mathcal{A}_D = R_D - R_D^0 = 0.0246$.

The produced pair number is

$$
N_{e^+e^-} = \sum_i N_{\gamma i} n_z l \sigma_{0i} S_{0i} \frac{4\beta}{\pi}, \tag{D5}
$$

which gives the standard deviation $\Delta R_{B,D} = 1/\sqrt{N_{e^+e^-}}$. Assuming an electron bunch with $N_{e^-}^0 = 1 \times 10^8$ is used for linear Compton scattering, the photon yield within 0.05 mrad is around $N_\gamma^0 = 0.5 \times 10^7$. Then, the confidence level for a single short could reach

$$
\begin{aligned}
n_B &= \frac{\mathcal{A}_B}{\Delta R_B} = \mathcal{A}_B \sqrt{\frac{4\beta n_z l}{\pi} \sum_i N_{\gamma i} \sigma_{0i} S_{0i}} = 8, \\
n_D &= \frac{\mathcal{A}_D}{\Delta R_D} = \mathcal{A}_D \sqrt{\frac{4\beta n_z l}{\pi} \sum_i N_{\gamma i} \sigma_{0i} S_{0i}} = 8,
\end{aligned} \tag{D6}
$$

indicating a single short measurement of vacuum polarization could reach a confidence level of 8σ.

Note that one should make sure that the observables $\mathcal{A}_B = 0.0247$ are much larger than the error of the initial photon polarization measurement $\sim \Delta R_B^0 = 1/\sqrt{N_{e^+e^-}^0} = 0.0035$ as $\xi_{10} \neq 0$ for initial γ rays. Apparently, the condition $\mathcal{A}_B - \Delta R_B^0 > \Delta R_B^0$ is fulfilled for a single shot. However, as for previous schemes [28], the feasibility relies on the capacity of postselection techniques to reduce the substantial background noise from radiation and cascaded detectors to enhance the conversion efficiency [66–68] and suppress multiple Coulomb scattering [69]. We emphasize that the experimental detection capacity for γ polarization (typically $\gtrsim 10\%$ [70]) is currently significantly lower than that for positrons (typically $\sim 0.5\%$ [71]).

[1] O. Halpern, Scattering processes produced by electrons in negative energy states, Phys. Rev. **44**, 855 (1933).

[2] V. Weisskopf, The electrodynamics of the vacuum based on the quantum theory of the electron, K. Dan. Vidensk. Selsk. Mat. Fys. Medd. **14**, 1 (1936).

[3] V. B. Berestetskii, E. M. Lifshitz, and L. P. Pitaevskii,, *Quantum Electrodynamics* (Pergamon Press, Oxford, 1982), Vol. 4.

[4] A. Ejlli, F. Della Valle, U. Gastaldi, G. Messineo, R. Pengo, G. Ruoso, and G. Zavattini, The PVLAS experiment: A 25 year effort to measure vacuum magnetic birefringence, Phys. Rep. **871**, 1 (2020).

[5] A. Cadène, P. Berceau, M. Fouchè, R. Battesti, and C. Rizzo, Vacuum magnetic linear birefringence using pulsed fields: Status of the BMV experiment, Eur. Phys. J. D **68**, 16 (2014).

[6] M. Marklund and P. K. Shukla, Nonlinear collective effects in photon-photon and photon-plasma interactions, Rev. Mod. Phys. **78**, 591 (2006).

[7] A. Di Piazza, C. Müller, K. Hatsagortsyan, and C. H. Keitel, Extremely high-intensity laser interactions with fundamental quantum systems, Rev. Mod. Phys. **84**, 1177 (2012).

[8] R. D. Peccei and H. R. Quinn, *CP* conservation in the presence of pseudoparticles, Phys. Rev. Lett. **38**, 1440 (1977).

[9] P. Sikivie, Experimental tests of the "invisible" axion, Phys. Rev. Lett. **51**, 1415 (1983).

[10] C. Schubert, Vacuum polarisation tensors in constant electromagnetic fields: Part I, Nucl. Phys. **B585**, 407 (2000).

[11] H. Gies, J. Jaeckel, and A. Ringwald, Polarized light propagating in a magnetic field as a probe for millicharged fermions, Phys. Rev. Lett. **97**, 140402 (2006).
[12] G. Zavattini, U. Gastaldi, R. Pengo, G. Ruoso, F. D. Valle, and E. Milotti, Measuring the magnetic birefringence of vacuum: The PVLAS experiment, Int. J. Mod. Phys. A **27**, 1260017 (2012).
[13] E. Zavattini, G. Zavattini, G. Ruoso, E. Polacco, E. Milotti, M. Karuza, U. Gastaldi, G. Di Domenico, F. Della Valle, R. Cimino *et al.*, Experimental observation of optical rotation generated in vacuum by a magnetic field, Phys. Rev. Lett. **96**, 110406 (2006).
[14] J. W. Yoon, Y. G. Kim, I. W. Choi, J. H. Sung, H. W. Lee, S. K. Lee, C. H. Nam, J. H. Sung, H. W. Lee, S. K. Lee, S. K. Lee, S. K. Lee, C. H. Nam, C. H. Nam, and C. H. Nam, Realization of laser intensity over 10^{23} W/cm^2, Optica **8**, 630 (2021).
[15] C. Danson, D. Hillier, N. Hopps, and D. Neely, Petawatt class lasers worldwide, High Power Laser Sci. Eng. **3**, e3 (2015).
[16] G. Geloni, E. Saldin, L. Samoylova, E. Schneidmiller, H. Sinn, T. Tschentscher, and M. Yurkov, Coherence properties of the European XFEL, New J. Phys. **12**, 035021 (2010).
[17] K. S. Schulze *et al.*, Towards perfectly linearly polarized X-rays, Phys. Rev. Res. **4**, 013220 (2022).
[18] A. Di Piazza, K. Z. Hatsagortsyan, and C. H. Keitel, Light diffraction by a strong standing electromagnetic wave, Phys. Rev. Lett. **97**, 083603 (2006).
[19] T. Heinzl, B. Liesfeld, K.-U. Amthor, H. Schwoerer, R. Sauerbrey, and A. Wipf, On the observation of vacuum birefringence, Opt. Commun. **267**, 318 (2006).
[20] F. Karbstein, Vacuum birefringence in the head-on collision of X-ray free-electron laser and optical high-intensity laser pulses, Phys. Rev. D **98**, 056010 (2018).
[21] T. N. Wistisen and U. I. Uggerhøj, Vacuum birefringence by Compton backscattering through a strong field, Phys. Rev. D **88**, 053009 (2013).
[22] V. Dinu, T. Heinzl, A. Ilderton, M. Marklund, and G. Torgrimsson, Vacuum refractive indices and helicity flip in strong-field QED, Phys. Rev. D **89**, 125003 (2014).
[23] See the HIBEF website: http://www.hzdr.de/db/Cms?pNid=427&pOid=35325.
[24] G. Cantatore, F. Della Valle, E. Milotti, L. Dabrowski, and C. Rizzo, Proposed measurement of the vacuum birefringence induced by a magnetic field on high energy photons, Phys. Lett. B **265**, 418 (1991).
[25] B. King and N. Elkina, Vacuum birefringence in high-energy laser-electron collisions, Phys. Rev. A **94**, 062102 (2016).
[26] A. Ilderton and M. Marklund, Prospects for studying vacuum polarisation using dipole and synchrotron radiation, J. Plasma Phys. **82**, 1 (2016).
[27] Y. Nakamiya and K. Homma, Probing vacuum birefringence under a high-intensity laser field with gamma-ray polarimetry at the GeV scale, Phys. Rev. D **96**, 053002 (2017).
[28] S. Bragin, S. Meuren, C. H. Keitel, and A. Di Piazza, High-energy vacuum birefringence and dichroism in an ultrastrong laser field, Phys. Rev. Lett. **119**, 250403 (2017).
[29] A. Apyan, R. Avakian, B. Badelek, S. Ballestrero, C. Biino, I. Birol, P. Cenci, S. Connell, S. Eichblatt, T. Fonseca *et al.*, Coherent bremsstrahlung, coherent pair production, birefringence, and polarimetry in the 20–170 GeV energy range using aligned crystals, Phys. Rev. ST Accel. Beams **11**, 041001 (2008).
[30] V. N. Baier, V. M. Katkov, V. M. Strakhovenko *et al.*, *Electromagnetic Processes at High Energies in Oriented Single Crystals* (World Scientific, Singapore, 1998).
[31] V. N. Baier, A. I. Milshtein, and V. M. Strakhovenko, Interaction between a photon and an intense electromagnetic wave, Zh. Eksp. Teor. Fiz. **69**, 1893 (1975).[Sov. Phys. JETP **42**, 961 (1975)].
[32] W. Becker and H. Mitter, Vacuum polarization in laser fields, J. Phys. A **8**, 1638 (1975).
[33] S. Meuren, C. H. Keitel, and A. Di Piazza, Polarization operator for plane-wave background fields, Phys. Rev. D **88**, 013007 (2013).
[34] G. Torgrimsson, Loops and polarization in strong-field QED, New J. Phys. **23**, 065001 (2021).
[35] B. King, T. Heinzl, and T. Blackburn, Strong field vacuum birefringence in plane wave pulses, Eur. Phys. J. C **83**, 901 (2023).
[36] C. Bula, K. T. McDonald, E. J. Prebys, C. Bamber, S. Boege, T. Kotseroglou, A. C. Melissinos, D. D. Meyerhofer, W. Ragg, D. L. Burke, R. C. Field, G. Horton-Smith, A. C. Odian, J. E. Spencer, D. Walz, S. C. Berridge, W. M. Bugg, K. Shmakov, and A. W. Weidemann, Observation of nonlinear effects in Compton scattering, Phys. Rev. Lett. **76**, 3116 (1996).
[37] D. L. Burke *et al.*, Positron production in multiphoton light-by-light scattering, Phys. Rev. Lett. **79**, 1626 (1997).
[38] C. Bamber *et al.*, Studies of nonlinear QED in collisions of 46.6 GeV electrons with intense laser pulses, Phys. Rev. D **60**, 092004 (1999).
[39] M. Altarelli, R. Assmann, F. Burkart, B. Heinemann, T. Heinzl, T. Koffas, A. Maier, D. Reis, A. Ringwald, and M. Wing, Summary of strong-field QED workshop, arXiv:1905.00059.
[40] N. Elkina, A. Fedotov, I. Y. Kostyukov, M. Legkov, N. Narozhny, E. Nerush, and H. Ruhl, QED cascades induced by circularly polarized laser fields, Phys. Rev. ST Accel. Beams **14**, 054401 (2011).
[41] C. P. Ridgers, J. G. Kirk, R. Duclous, T. Blackburn, C. S. Brady, K. Bennett, T. Arber, and A. Bell, Modelling gamma-ray photon emission and pair production in high-intensity laser–matter interactions, J. Comput. Phys. **260**, 273 (2014).
[42] D. Green and C. Harvey, Simla: Simulating particle dynamics in intense laser and other electromagnetic fields via classical and quantum electrodynamics, Comput. Phys. Commun. **192**, 313 (2015).
[43] A. Gonoskov, S. Bastrakov, E. Efimenko, A. Ilderton, M. Marklund, I. Meyerov, A. Muraviev, A. Sergeev, I. Surmin, and E. Wallin, Extended particle-in-cell schemes for physics in ultrastrong laser fields: Review and developments, Phys. Rev. E **92**, 023305 (2015).
[44] Y.-Y. Chen, P.-L. He, R. Shaisultanov, K. Z. Hatsagortsyan, and C. H. Keitel, Polarized positron beams via intense two-color laser pulses, Phys. Rev. Lett. **123**, 174801 (2019).

[45] Y.-F. Li, Y.-Y. Chen, W.-M. Wang, and H.-S. Hu, Production of highly polarized positron beams via helicity transfer from polarized electrons in a strong laser field, Phys. Rev. Lett. **125**, 044802 (2020).
[46] Y.-N. Dai, B.-F. Shen, J.-X. Li, R. Shaisultanov, K. Z. Hatsagortsyan, C. H. Keitel, and Y.-Y. Chen, Photon polarization effects in polarized electron–positron pair production in a strong laser field, Matter Radiat. Extremes **7**, 014401 (2022).
[47] K.-H. Zhuang, Y.-Y. Chen, Y.-F. Li, K. Z. Hatsagortsyan, and C. H. Keitel, Laser-driven lepton polarization in the quantum radiation-dominated reflection regime, Phys. Rev. D **108**, 033001 (2023).
[48] Y.-Y. Chen, K. Z. Hatsagortsyan, C. H. Keitel, and R. Shaisultanov, Electron spin-and photon polarization-resolved probabilities of strong-field QED processes, Phys. Rev. D **105**, 116013 (2022).
[49] Y.-F. Li, Y.-Y. Chen, K. Z. Hatsagortsyan, A. Di Piazza, M. Tamburini, and C. H. Keitel, Strong signature of one-loop self-energy in polarization resolved nonlinear Compton scattering, Phys. Rev. D **107**, 116020 (2023).
[50] K. Yokoya and P. Chen (private communication).
[51] A. Gonsalves, K. Nakamura, J. Daniels, C. Benedetti, C. Pieronek, T. De Raadt, S. Steinke, J. Bin, S. Bulanov, J. Van Tilborg *et al.*, Petawatt laser guiding and electron beam acceleration to 8 GeV in a laser-heated capillary discharge waveguide, Phys. Rev. Lett. **122**, 084801 (2019).
[52] N. Muramatsu, M. Yosoi, T. Yorita, Y. Ohashi, J. Ahn, S. Ajimura, Y. Asano, W. Chang, J. Chen, S. Daté *et al.*, Spring-8 LEPS2 beamline: A facility to produce a multi-GeV photon beam via laser Compton scattering, Nucl. Instrum. Methods Phys. Res., Sect. A **1033**, 166677 (2022).
[53] I. C. E. Turcu *et al.*, High field physics and QED experiments at ELI-NP, Rom. Rep. Phys. **68**, S145 (2016).
[54] N. Zamfir, Nuclear physics with 10 PW laser beams at extreme light infrastructure–nuclear physics (ELI-NP), Eur. Phys. J. Special Topics **223**, 1221 (2014).
[55] M. Beckmann, A. Borissov, S. Brauksiepe, F. Burkart, H. Fischer, J. Franz, F. Heinsius, K. Königsmann, W. Lorenzon, F. Menden *et al.*, The longitudinal polarimeter at HERA, Nucl. Instrum. Methods Phys. Res., Sect. A **479**, 334 (2002).
[56] I. Passchier, D. W. Higinbotham, C. de Jager, B. Norum, N. Papadakis, and N. Vodinas, A Compton backscattering polarimeter for measuring longitudinal electron polarization, Nucl. Instrum. Methods Phys. Res., Sect. A **414**, 446 (1998).
[57] S. Escoffier, P. Bertin, M. Brossard, E. Burtin, C. Cavata, N. Colombel, C. de Jager, A. Delbart, D. Lhuillier, F. Marie *et al.*, Accurate measurement of the electron beam polarization in JLab Hall A using Compton polarimetry, Nucl. Instrum. Methods Phys. Res., Sect. A **551**, 563 (2005).
[58] D. Jones, J. Napolitano, P. Souder, D. King, W. Henry, D. Gaskell, and K. Paschke, Accurate determination of the electron spin polarization in magnetized iron and nickel foils for Møller polarimetry, Nucl. Instrum. Methods Phys. Res., Sect. A **1043**, 167444 (2022).
[59] J. Arrington, E. Beise, B. Filippone, T. O'Neill, W. Dodge, G. Dodson, K. Dow, and J. Zumbro, A variable energy Møller polarimeter at the mit-bates linear accelerator center, Nucl. Instrum. Methods Phys. Res., Sect. A **311**, 39 (1992).
[60] C. Møller, Zur theorie des durchgangs schneller elektronen durch materie, Ann. Phys. (N.Y.) **406**, 531 (1932).
[61] F. Negoita, M. Roth, P. G. Thirolf, S. Tudisco, F. Hannachi, S. Moustaizis, I. Pomerantz, P. McKenna, J. Fuchs, K. Sphor *et al.*, Laser driven nuclear physics at ELINP, arXiv:2201.01068.
[62] A. Li, C. Qin, H. Zhang, S. Li, L. Fan, Q. Wang, T. Xu, N. Wang, L. Yu, Y. Xu *et al.*, Acceleration of 60 MeV proton beams in the commissioning experiment of the SULF-10 PW laser, High Power Laser Sci. Eng. **10**, e26 (2022).
[63] Y.-F. Li, Y.-Y. Chen, K. Z. Hatsagortsyan, and C. H. Keitel, Helicity transfer in strong laser fields via the electron anomalous magnetic moment, Phys. Rev. Lett. **128**, 174801 (2022).
[64] V. N. Baier, V. M. Katkov, and V. M. Strakhovenko, *Electromagnetic Processes at High Energies in Oriented Single Crystals* (World Scientific, Singapore, 1998).
[65] H. A. Olsen and L. C. Maximon, Photon and electron polarization in high-energy bremsstrahlung and pair production with screening, Phys. Rev. **114**, 887 (1959).
[66] M. Tavani *et al.*, The AGILE instrument, Proc. SPIE **4851**, 1151 (2003).
[67] W. Atwood, A. A. Abdo, M. Ackermann, W. Althouse, B. Anderson, M. Axelsson, L. Baldini, J. Ballet, D. Band, G. Barbiellini *et al.*, The large area telescope on the fermi gamma-ray space telescope mission, Astrophys. J. **697**, 1071 (2009).
[68] T. Peitzmann, Prototype studies for a forward em calorimeter in ALICE, arXiv:1308.2585.
[69] P. Gros and D. Bernard, Gamma-ray polarimetry with conversions to e^+e^- pairs: Polarization asymmetry and the way to measure it, Astropart. Phys. **88**, 30 (2017).
[70] K. Ozaki, S. Takahashi, S. Aoki, K. Kamada, T. Kaneyama, R. Nakagawa, and H. Rokujo, Demonstration of polarization sensitivity of emulsion-based pair conversion telescope for cosmic gamma-ray polarimetry, Nucl. Instrum. Methods Phys. Res., Sect. A **833**, 165 (2016).
[71] A. Narayan *et al.*, Precision electron-beam polarimetry at 1 GeV using diamond microstrip detectors, Phys. Rev. X **6**, 011013 (2016).